International Journal of Multiphase Flow 152 (2022) 104065

Contents lists available at ScienceDirect

International Journal of Multiphase Flow

journal homepage: www.elsevier.com/locate/ijmulflow

Effect of roughness on elongated particles in turbulent channel flow

Domenico Saccone [a,*], Cristian Marchioli [b,c], Mauro De Marchis [a]

[a] Facoltà di Ingegneria e Architettura, Università di Enna Kore, Italy
[b] Dipartimento Politecnico di Ingegneria e Architettura, Università di Udine, Italy
[c] Dipartimento di Fluidodinamica, CISM di Udine, Italy

ARTICLE INFO

Keywords:
Multiphase flow
Direct numerical simulation
Lagrangian Particle Tracking
Turbulence
Roughness
Fiber transport

ABSTRACT

In this paper, we examine the deposition and resuspension of rigid elongated particles transported by turbulence in a channel bounded by two-dimensional roughness. To analyze these processes, we use an Euler–Lagrange approach based on Direct Numerical Simulation of the carrier phase and Lagrangian Particle Tracking of the dispersed phase. Four different channel configurations are considered: One is the classical channel flow bounded by smooth flat walls, whereas the other three correspond to a channel with walls of increasing roughness. The roughness shape is obtained by superimposition of sinusoidal functions with different amplitude k and is characterized by the mean absolute value of the amplitude, $\bar{k} = 0.012$, 0.024 and 0.050 ($\bar{k} = 0$ for a smooth wall). The friction Reynolds number is $Re_\tau = 150$ for all cases. Particles are modeled as prolate ellipsoids and classified according to their aspect ratio λ. Three different particles sets are considered: $\lambda = 1$, corresponding to the reference case of spheres, $\lambda = 3$, corresponding to slightly elongated particles, and $\lambda = 10$, corresponding to long fiber-like particles. The particle response time is $St^+ = 5$ for all sets. In turbulent flow bounded by smooth walls, particles are known to accumulate preferentially in the near-wall region, leaving the central region of the channel scarcely populated. Wall roughness produces a completely different scenario: Particles exhibit a more homogeneous distribution along the wall-normal direction. We show that the aspect ratio does not affect the preferential distribution and the velocity statistics of the particles. The effect of elongation, however, becomes important for their preferential orientation, which is much weaker than in the smooth-walls case, in the near-wall region, while recovering the smooth-walls case in the outer region of the channel. This finding supports the validity of Townsend's similarity hypothesis, namely that the bulk flow dynamics are unaffected by the roughening of the bounding walls.

1. Introduction

The processes of non-spherical particle transport, deposition and resuspension by a turbulent flow play a crucial role in a wide variety of industrial and environmental applications. Examples of technological interest include slurry pipeline transport (Chen et al., 2020), pulp- and paper-making (Lundell et al., 2011) or combustion of pulverized coal (Wang et al., 2020), while sediment transport in rivers (Burns and Meiburg, 2015; D'Alessandro et al., 2021) or pollution control problems (Benedini, 2020; Chandrappa and Das, 2021) are just some of the many instances that are relevant for the environment. Regardless of the specific application, the flow field in which particles evolve is almost always turbulent and bounded by solid walls; this introduces inhomogeneities and intermittency in the flow, which have a strong impact on particle-turbulence interactions and, in turn, make particle transport, deposition and resuspension particularly complex to study. Current physical understanding of wall-bounded, particle-laden turbulent flows has relied heavily on experiments (Sumbekova et al., 2017; Fong et al., 2019) and simulations in which dilute suspensions of sub-Kolmogorov spherical heavy particles are considered (Lucci et al., 2010).[1] Limiting our discussion to simulations, the main advantage associated with the study of this class of particles is that particles can be modeled as Lagrangian points whose trajectory stems directly from the solution of a rather simple equation of translational motion, with

* Corresponding author.
E-mail address: domenico.saccone@unikorestudent.it (D. Saccone).

[1] The most detailed numerical approach currently available is the particle-resolved approach, which solves for the flow around each particle prescribing exact boundary conditions for forces and torques at the particle surface. However, the computational cost associated with the calculation of such boundary conditions restricts the application of this approach to relatively small numbers of particles. Hence, this approach is not yet suitable to study large swarms of particles as those considered in this study. For this reason, we do not include a discussion on particle-resolved simulations here and we refer the reader to Riemer et al. (2009) and Tenneti and Subramaniam (2014).

https://doi.org/10.1016/j.ijmultiphaseflow.2022.104065
Received 28 June 2021; Received in revised form 8 February 2022; Accepted 16 March 2022
Available online 30 March 2022

no need to account for the rotational dynamics of the particle (Balachandar, 2009). In spite of the simplifications, Eulerian–Lagrangian approaches based on this methodology have helped in shedding light on the connection between inertia-driven fluid–particle interactions and clustering processes, due to the formation of strong inhomogeneities in particle spatial distribution (Balachandar and Eaton, 2010; Sozza et al., 2020) and to the occurrence of different segregation mechanisms such as the centrifugal expulsion of particles from the core of the eddies (Maxey, 1987) or the sticking property of zero-acceleration points of the carrier flow (Goto and Vassilicos, 2008; Coleman and Vassilicos, 2009). In inhomogeneous turbulent flows, large-scale clusters are found to result from the migration of the particles in regions of lower turbulence intensity occur, a phenomenon usually referred to as turbophoresis (Reeks, 1983; Marchioli and Soldati, 2002). In the case of confined flows, these regions are the near-wall ones, where strong and persistent spatial modulations of the turbulent intensity are generated. Once trapped inside the viscous sublayer, particle distribution exhibits a spanwise inhomogeneity that is due to the streaky structure of the fluid velocity field (Rouson and Eaton, 2001; Marchioli and Soldati, 2002). All of these preferential concentration phenomena scale with a single parameter when particles are much heavier than the carrier fluid: This parameter is the particle response time, referred to as Stokes number when made dimensionless using the fluid characteristic time scale (Soldati and Marchioli, 2009; Sardina et al., 2011; Ji et al., 2013, 2014).

Fluid–particle interactions, however, are known to also depend on the shape of the dispersed particles, which may easily deviate from that of a sphere. Indeed, all the above-mentioned applications are characterized by the presence of particles with non-spherical (and possibly irregular) shape, that exhibit specific drag characteristics (Voth and Soldati, 2017; Connolly et al., 2020). Shapes effects on particle transport in fluid flows, both viscous and turbulent, have been studied extensively in a huge number of theoretical works (see Jeffery (1922), Maxey and Riley (1983) and Brenner (1963) among others), laboratory experiments (Eaton and Fessler, 1994; Parsheh et al., 2005; Alipour et al., 2021) and numerical simulations (e.g. Fan and Ahmadi (1995), Marchioli and Soldati (2002), Balachandar and Eaton (2010), Brandt et al. (2011), Marchioli et al. (2016), Qiu et al. (2019) and Jain et al. (2020) to name a few). Focusing again on simulations, non-spherical particles are more complex to model than spherical ones in view of the strong coupling between translational and rotational motion and because of the difficulty in deriving suitable models for the hydrodynamic forces acting on the particles, in view of the extremely broad range of geometries that a non-spherical shape may encompass (Voth and Soldati, 2017; Connolly et al., 2020). To simplify computational complexity, most of the simulations have been carried out considering mathematically-treatable shapes like prolate or oblate ellipsoids (see Voth and Soldati (2017) for a comprehensive review). Ellipsoids have no geometrical discontinuity and can be classified by their aspect ratio, defined as the ratio between the major axis and the minor axis of the particle (and referred to as λ hereinafter). Using this approach, and assuming that particles could still be treated as points, Zhang et al. (2001) were among the first to perform Eulerian–Lagrangian calculations of ellipsoidal particle dispersion in turbulent channel flow, and explore the combined effect of particle elongation and inertia on preferential concentration and wall accumulation phenomena. Mortensen et al. (2008) and Marchioli et al. (2010) used the same methodology to study the behavior of ellipsoidal particles with aspect ratio up to $\lambda = 50$ and response time up to $St^+ = 30$ (for which the inertial bias on spatial distribution is significant). Because of the point-particle assumption, elongated particles were found to segregate in the low-speed fluid streaks within the viscous sublayer, similarly to spherical particles, showing the dominant effect of inertia (over elongation) on preferential concentration and wall accumulation. Besides the spatial distribution, an important and widely-examined observable phenomena is the orientation attained by the particles within the flow domain. A distinctive feature highlighted in several studies (see Marchioli et al. (2010), Challabotla et al. (2016) and Arcen et al. (2017) among others) is the preferential alignment that particles exhibit along the mean flow direction once they evolve within the near-wall region. No such alignment is observed in the core of the flow, where the particles tend to orient themselves in a more uniform fashion.

Particles at the channel center (where turbulence is nearly isotropic) and near the wall (where the flow becomes highly sheared) show different rotational dynamics and surprisingly different effects of particle inertia are noted. In the bulk of the flow, oblate particles tend to rotate orthogonally to their symmetry axes, whereas prolate particles rotate around their symmetry axes (see Zhao and van Wachem (2013), Zhao et al. (2015), Arcen et al. (2017) and Marchioli et al. (2019), among others). This trend is weakened by increasing inertia so that highly inertial oblate spheroids rotate nearly isotropically about their principle axes. Near the walls, inertia does not shift the rotation of spheroids towards isotropy but, rather, reverses the trend, causing oblate spheroids to rotate strongly about their symmetry axes and prolate spheroids to rotate normal to their symmetry axes. The orientational behavior of the particles in the anisotropic turbulence field near a shear-free wall is qualitatively different. Direct comparisons between the orientation statistics near a sheared wall and near a shear-free wall provide an insight into the role played by the mean shear. Yang et al. (2020) observed that disks (resp. rods) with low inertia preferentially oriented in the directions of Lagrangian compression (resp. stretching) of the fluid elements, in a way that is similar to that already reported for tracer spheroids. Spheroids with intermediate inertia are found to exhibit similar orientations as the low-inertia particles near the shear-free wall, although the behavior of such spheroids appears to be greatly affected by inertia near the sheared wall. The most inertial spheroids, however, tend to orient themselves almost randomly near the shear-free wall, a finding that can be ascribe to the absence of mean shear and inertial filtering of the anisotropic vorticity field. For the channel flow case, Cui et al. (2020) examined how the distribution of relative angles between a rod and the Lagrangian stretching direction depends on the aspect ratio of the rod and upon the distance of the rod from the channel wall, finding that this distribution exhibits two regimes: a plateau at small angles corresponding to random uncorrelated motion, and power-law tails due to large excursions. Slender rods near the channel center are found to align better with the Lagrangian stretching direction compared with those near the channel wall, in a way that can be explained in terms of simple statistical models based on Jeffery's equation: Qualitatively near the channel center and quantitatively near the channel wall. More recently, some researches (see among others Zhang et al. (2020) and Jain et al. (2021)) performed particle-resolved simulations of bedload sediment transport in open channel flow. Considering the different simulation methodology and flow configurations adopted by these Authors, it seems reasonable to conclude that the tendency to orient in a preferred direction near a wall is a universal feature of non-spherical particles. This tendency, which is found to persist over a significant amount of time during the dispersion (Marchioli et al., 2010), clearly provides the particles with a source of anisotropy that adds to that of the flow.

Cui et al. (2021) numerically studied the angular dynamics of small rigid fibers and disks in turbulent channel flow, focusing on interactions between particles and near-wall coherent vortices. These Authors found three distinct alignment patterns that fibers and disks can attain around ensemble-averaged vortices. From the wall to the channel center a shear-dominated region, a structure-dominated region, and an isotropic region, each with its unique alignment pattern can be observed.

All of the studies just examined, were performed considering archetypal flow domains bounded by smooth walls. In many real life situations, however, the actual flow is bounded by irregular rough walls. This is particularly true in environmental applications, where bounding surfaces often exhibit non-negligible spatial heterogeneity.

Rough surfaces are known to modify the physical and statistical properties of turbulence, depending on the relationship between the dominant length-scales of the surface and those of the flow: when the dominant length-scales of the surface become comparable to the dominant length-scale of the flow (e.g. the boundary layer thickness), then the flow also exhibits large-scale spatial heterogeneity that is locked-on to the surface heterogeneity. For further details, the reader is referred to Napoli et al. (2008), Volino et al. (2011) and De Marchis et al. (2015). Perhaps the main macroscopic effect of large-scale roughness is the downward shift of the mean velocity profile in the logarithmic region, known as Roughness Function: it has been demonstrated that this shift is highly dependent on the geometric parameters of the wall roughness (De Marchis et al., 2020). The effect of roughness on the dynamics of a solid dispersed phase in a turbulent flow has been investigated in a number of studies, all dealing with spherical particles.

Among one-way coupled simulations, Milici et al. (2014) studied the particle-laden turbulent flow in a channel bounded by irregular two-dimensional rough surfaces and compared their results with those obtained for classical flat-wall model, showing that wall roughness produces completely different volumetric concentration statistics with respect to the case of smooth walls. This happens because particles are redistributed throughout the entire channel by roughness: So they tend to avoid the near-wall region and populate the center of the channel (De Marchis et al., 2017; Luo et al., 2019). Later (De Marchis and Milici, 2016), observed the effect rough walls on particle dispersion in two-way coupling approach. Apparently, different transport mechanisms set in along the direction of gravity, in view of the different features that characterize the coherent flow structures in the two configurations. We remark here that other studies in archival literature have considered small-scale roughness, namely roughness that scales with the size of the particles and does not affect the flow. For instance, Vreman (2015) examined the different attenuation of turbulence induced in particle-laden smooth and rough channel flows, whereas Mallouppas and van Wachem (2013), who were able to demonstrate that rough walls and inter-particle collisions have an important effect in redistributing the particles across the channel, even for very dilute flows. This type of roughness, however, is not relevant for the physical problem and flow configuration examined here. For this reason, it will not be discussed further. In view of the brief literature review provided so far, it appears that a thorough combined analysis of roughness effects and particle shape effects on the turbulent transport of a dispersed suspension is missing. The aim of the present study is precisely to fill this gap. In particular, we want to analyze the dynamics of elongated particles, modeled as prolate ellipsoids (e.g. to mimic sediment grains in a water stream) in a complex flow domain bounded by two-dimensional rough surfaces. Focus of this analysis is on the effect of roughness on particle spatial distribution and preferential orientation, especially in the near-wall region. In addition, the effect of the particle aspect ratio, which is expected to introduce at least a quantitative change in the statistical observables of interest, is discussed. By doing so, we aim at assessing the relative importance of the channel roughness and particle length. The paper is organized as follows. The governing equations and the numerical methodology used for the simulations are provided in Section 2. Section 3 reports details on the computational domains and the simulation parameters, whereas Section 4 is devoted to the analysis and discussion of the fluid and particle statistics, in conclusion the main final remarks and considerations are drawn in Section 5.

2. Computational methodology

The computational methodology adopted in this work is based on an Eulerian flow solver, which performs Direct Numerical Simulation of turbulence and has been widely validated in previous works (see De Marchis et al. (2010, 2015), De Marchis (2012) and De Marchis et al. (2019), for instance), and on a Lagrangian particle tracker that has been also used in a number of previous DNS-based works (see Mortensen et al. (2008), Marchioli et al. (2010, 2016), Arcen et al. (2017) and Michel and Arcen (2021) among others). The rationale behind the choice of such methodology is that we want to compare as directly as possible our results with those obtained for the same kind of ellipsoidal particles in the case of channel flow bounded by smooth walls. Therefore, the Eulerian fluid dynamics is governed by the Continuity and Navier–Stokes equations, formulated for an incompressible Newtonian fluid:

$$\frac{\partial u_i}{\partial t}+\frac{\partial u_i u_j}{\partial x_j}-\frac{1}{Re_\tau}\frac{\partial^2 u_i}{\partial x_j \partial x_j}+\frac{\partial p}{\partial x_i}+\Pi\delta_{i1}=0; \qquad \frac{\partial u_i}{\partial x_i}=0 \quad i=1,\ldots,3 \tag{1}$$

where u_i is the *ith* dimensionless velocity component, x_i is the *ith* non-dimensional coordinate, p is the kinematic pressure field, Π is the imposed mean non-dimensional pressure gradient that drives the flow, δ_{i1} is the Kronecker function and, finally, $Re_\tau = u_\tau \delta/\nu$, is the friction Reynolds number, with u_τ the friction (or shear) velocity, δ the channel half-width and ν the fluid kinematic viscosity.

Direct Numerical Simulations of the flow were carried out at $Re_\tau = 150$, using the 3D numerical model PANORMUS (PArallel Numerical Open-souRce Model for Unsteady flow Simulation, http://www.panormus3d.org), which is second order accurate both in time and space. The model uses an explicit Adams–Bashforth method for the time advancement of the solution, while a fractional-step technique is used to overcome the pressure–velocity decoupling typical of incompressible flows. The value chosen for the flow Reynolds number corresponds to a physical instance in which air with $\nu = 1.5710^{-5}$ m^2/s flows at bulk velocity $u_b = 1.65$ m s^{-1} in a 4-cm high channel or fresh water with $\nu = 10^{-6}$ m^2/s flows at bulk velocity $u_b = 0.35$ m s^{-1} in a 6-cm high channel. We remark here that, even though the Eulerian solver has been applied and validated up to value of friction Reynolds number equal to 1000 (see De Marchis et al. (2020) for more details), in the present study, the imposed friction Reynolds number was kept equal to 150 to allow direct comparison with results in archival literature (in particular, Mortensen et al. (2008), Marchioli et al. (2010), Marchioli and Soldati (2013) and Michel and Arcen (2021)), and hence single out the interplay between particle inertia and wall roughness, which represents the main objective of our work. The effect of the Reynolds number on the concentration and preferential orientation of inertial ellipsoids in smooth-wall channel flow has been analyzed by Michel and Arcen (2021) who observed that a longer time transient is required to achieve a steady-state wall-normal concentration at increasing Re_τ and that the main effect of such an increase is observed on preferential orientation (due to stronger fluid vorticity fluctuations that act to destabilize the weakly-stable rotation orbits of the ellipsoids). Interestingly, the concentration profiles very close to the wall are practically unaffected by the Reynolds number for a given aspect ratio and particle Stokes number. It could be inferred that the presence of rough walls might induce some Re_τ-dependence of concentration, but analyzing such dependence is beyond the scope of our study: Rather, it could represent a possible future development.

The solid phase dispersed in the channel consists of prolate ellipsoidal particles with aspect ratio $\lambda = b/a$, were a is the semi-minor axis and b being the semi-major axis of the ellipsoid. The translational equation of motion of an individual particle is given by the linear momentum equation:

$$\mathrm{d}\mathbf{v}_p/\mathrm{d}t = \mathbf{F}/m\ , \tag{2}$$

where $\mathbf{v}_p$ is the particle velocity, $\mathbf{F}$ is the total hydrodynamic drag force acting on the particle, and $m = (4/3)\pi a^3 \lambda \rho_p$ is the particle mass, with ρ_p the particle density. The expression for $\mathbf{F}$ used in our simulations was first derived by Brenner (1963) for an ellipsoid under creeping flow conditions:

$$\mathbf{F} = \mu\,\mathbf{K}\,(\mathbf{u}_p - \mathbf{v}_p)\ , \tag{3}$$

where μ is the fluid dynamic viscosity, $\mathbf{K}$ is the resistance tensor and $\mathbf{u}_p$ is the fluid velocity at particle position. It is worthwhile to mention

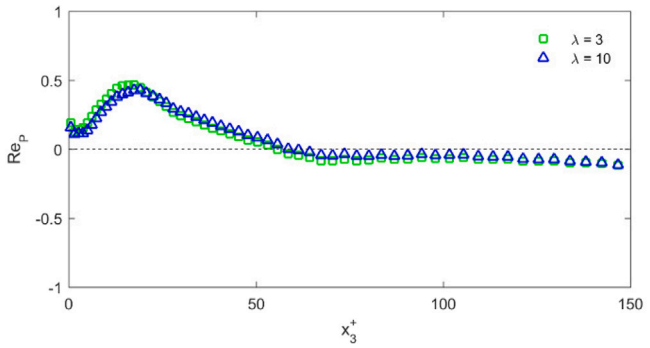

Fig. 1. Fiber Reynolds number, Re_p, for $\lambda = 3$ (squares) and $\lambda = 10$ (triangles), as a function of the wall-normal coordinate, x_3^+.

that the expression for the hydrodynamic drag force derived by Brenner (1963) is valid in the limit of small fiber Reynolds number, $Re_p = 2a|u_{rel}|/\nu$, with a the fiber cross-sectional radius and u_{rel} the relative velocity between the fiber and the surrounding fluid, evaluated at the fiber's center of mass. In this limit, the flow around the particle is Stokesian and fluid inertia can be ignored. As shown in Fig. 1 Re_p is always smaller than unity, even well inside the buffer region. This indicates that the condition of creeping flow around the fiber is adequately satisfied if the fiber Reynolds number is defined based on the semi-minor axis of the fiber. An effective particle Reynolds number might be higher than Re_p based on the mean slip velocity, partly because $2a$ is the shortest geometrical length scale of a prolate ellipsoid and partly because the instantaneous slip velocity may exceed the mean slip velocity, as pointed out by Zhao et al. (2014) for spherical particles. Several correction formulas exist to account for finite-Reynolds-number effects on the motion of spherical particles but, no such corrections (e.g. Schiller–Naumann-like corrections) yet exist for non-spherical particles, as also discussed in Marchioli et al. (2016). Development of finite-Reynolds-number corrections for the drag force, but also for the torque acting from the viscous fluid on ellipsoidal particles, is indeed welcome as it would make the Lagrangian particle modeling way more versatile.

The resistance tensor $\mathbf{K}$ is expressed with respect to the Eulerian (inertial) frame of reference, $\mathbf{x} = \langle x_1, x_2, x_3 \rangle$, but is first calculated with respect to the Lagrangian frame of reference, $\mathbf{x}' = \langle x_1', x_2', x_3' \rangle$, attached to the ellipsoid with origin at the ellipsoid's center of mass, as shown in Fig. 2. Also shown in this Figure is the co-moving frame of reference, $\mathbf{x}'' = \langle x_1'', x_2'', x_3'' \rangle$, attached to the ellipsoid with origin at its center of mass and axes parallel to the inertial frame. This frame is used to identify the orientation of the ellipsoid. Using these frames, the resistance tensor is computed as $\mathbf{K} = \mathbf{A}^t\mathbf{K}'\mathbf{A}$, where $\mathbf{K}'$ is the resistance tensor computed in the fiber frame, $\mathbf{A}$ is the orthogonal transformation matrix comprising the direction cosines (which, in turn, are defined by the Euler parameters), and $\mathbf{A}^t$ is its transpose. Matching the x_1', x_2', x_3' axes with the principal axes of resistance, tensor $\mathbf{K}'$ can be computed in diagonal form as:

$$\mathbf{K}' = \begin{bmatrix} k_{x_1'x_1'} & 0 & 0 \\ 0 & k_{x_2'x_2'} & 0 \\ 0 & 0 & k_{x_3'x_3'} \end{bmatrix}, \tag{4}$$

where the diagonal elements read as:

$$k_{x_1'x_1'} = k_{x_2'x_2'} = \frac{16(\lambda^2-1)^{3/2}}{[(2\lambda^2-3)\ln(\lambda+\sqrt{\lambda^2-1})]+\lambda\sqrt{\lambda^2-1}},$$

$$k_{x_3'x_3'} = \frac{8(\lambda^2-1)^{3/2}}{[(2\lambda^2-1)\ln(\lambda+\sqrt{\lambda^2-1})]+\lambda\sqrt{\lambda^2-1}}, \tag{5}$$

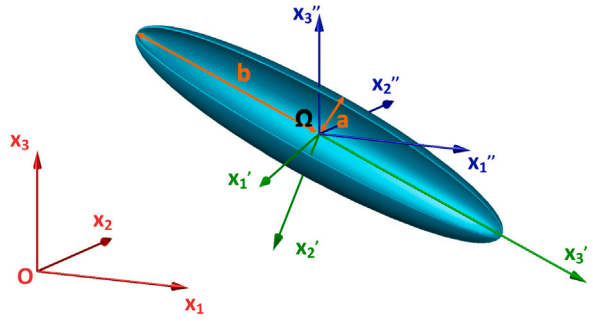

Fig. 2. Reference frames used to describe the motion of an ellipsoidal particle.

The complete set of equations considered to describe the translational and rotational motion of the particles, in dimensionless form, reads as Marchioli et al. (2010):

$$\textit{Kinematics} \quad \begin{cases} \dfrac{d\mathbf{x}_{p,(G)}}{dt} = \mathbf{v}_p \\ \dfrac{de_0}{dt} = \dfrac{1}{2}(-e_1\omega_{x_1'} - e_2\omega_{x_2'} - e_3\omega_{x_3'}) \\ \dfrac{de_1}{dt} = \dfrac{1}{2}(e_0\omega_{x_1'} - e_3\omega_{x_2'} + e_2\omega_{x_3'}) \\ \dfrac{de_2}{dt} = \dfrac{1}{2}(e_3\omega_{x_1'} + e_0\omega_{x_2'} - e_1\omega_{x_3'}) \\ \dfrac{de_3}{dt} = \dfrac{1}{2}(-e_2\omega_{x_1'} + e_1\omega_{x_2'} + e_0\omega_{x_3'}) \end{cases} \tag{6}$$

$$\textit{Dynamics} \quad \begin{cases} \dfrac{d\mathbf{v}_p}{dt} = \dfrac{3}{4\lambda Sa^2}\mathbf{K}\cdot(\mathbf{u}_p - \mathbf{v}_p) \\ \dfrac{d\omega_{x_1'}}{dt} = \omega_{x_2'}\omega_{x_3'}\left(1 - \dfrac{2}{1+\lambda^2}\right) + \dfrac{20\left[(1-\lambda^2)f' + (1+\lambda^2)(\xi' - \omega_{x_1'})\right]}{(\alpha_0 + \lambda^2\gamma_0)(1+\lambda^2)Sa^2} \\ \dfrac{d\omega_{x_2'}}{dt} = \omega_{x_1'}\omega_{x_3'}\left(\dfrac{2}{1+\lambda^2} - 1\right) + \dfrac{20\left[(\lambda^2-1)g' + (\lambda^2+1)(\eta' - \omega_{x_2'})\right]}{(\alpha_0 + \lambda^2\gamma_0)(1+\lambda^2)Sa^2} \\ \dfrac{d\omega_{x_3'}}{dt} = \dfrac{20}{(2\alpha_0)Sa^2}(\chi' - \omega_{x_3'}) \end{cases} \tag{7}$$

where $\mathbf{x}_{p,(G)}$ is the ellipsoid's location vector (centered at the center of mass $\mathbf{G}$ of the ellipsoid), e_i are the Euler parameters, ω_{x_i} is the ith component of the ellipsoid's angular velocity, and S is the particle-to-fluid density ratio. The parameters α_0 and γ_0 were derived by Jeffery (1922) to compute the torque components for an ellipsoid subjected to linear shear under creeping flow conditions. The quantities f', g', ξ', η' and χ' are the elements of the fluid's rate of strain tensor and of rotation tensor, all expressed in the particle frame. Eqs. (6) are integrated in time using a standard fourth-order Runge–Kutta scheme, while Eqs. (7) are solved using a mixed explicit/implicit differencing procedure developed by Fan and Ahmadi (1995). The Lagrangian particle tracking code interpolates fluid velocities at discrete grid nodes onto the particle position, and with this velocity the equations of motion of the particle are integrated in time. The same time-step size as that of the fluid is used for integration. For each particle and each time-step, the Euler parameters are renormalized according to:

$$e_i = \frac{e_i}{\sqrt{e_0^2 + e_1^2 + e_2^2 + e_3^2}}, \tag{8}$$

to preserve the constraint $e_0^2 + e_1^2 + e_2^2 + e_3^2 = 1$.

In our simulations, we did not include the effect of gravity on the particles. This was done to allow a direct comparison of our results,

Table 1
Details of all cases: Re_τ is the friction Reynolds number , Lx_1, Lx_2 and Lx_3 are the domain sizes; Nx_1, Nx_2 and Nx_3 are the number of cells; Δx_1^+, Δx_2^+, $\Delta x_{3,min}^+$ and $\Delta x_{3,max}^+$ are the mesh resolution. Superscript $^+$ is used to indicate variables in wall units, obtained using the fluid viscosity ν and the friction velocity u_τ.

Case	Re_τ	Lx_1	Lx_2	Lx_3	Nx_1	Nx_2	Nx_3	Δx_1^+	Δx_2^+	$\Delta x_{3,min}^+$	$\Delta x_{3,max}^+$
F1	150	$2\pi\delta$	$\pi\delta$	2δ	128	128	128	7.4	3.7	0.096	5.9
R1	150	$4\pi\delta$	$\pi\delta$	2δ	256	128	128	7.4	3.7	0.048	6.4
R2	150	$4\pi\delta$	$\pi\delta$	2δ	256	128	128	7.4	3.7	0.048	6.4
R3	150	$4\pi\delta$	$\pi\delta$	2δ	256	128	128	7.4	3.7	0.048	6.4

Table 2
Geometric parameters of the rough walls: $\bar{k}/\delta$ and $\bar{k}^+$ are the averaged absolute deviation of the heights of the rough walls, k_s/δ and k_s^+ are the equivalent sand-grain roughness, k_{max}/δ and k_{max}^+ are the highest roughness peaks and ES is the Effective slope of roughness. ΔU^+ is the roughness function, discussed in Section 4.

Case	Type	$\bar{k}/\delta$	$\bar{k}^+$	k_s/δ	k_s^+	k_{max}/δ	k_{max}^+	ES	ΔU^+
F1	Smooth	–	–	–	–	–	–	–	–
R1	2D	0.012	1.8	0.23	34.5	0.027	4.05	0.04	1.15
R2	2D	0.024	3.6	0.29	43.5	0.065	9.75	0.09	1.80
R3	2D	0.050	7.5	0.49	67.5	0.135	20.25	0.20	4.18

which highlight the role played by roughness, with those obtained in previous DNS-based studies for the case of smooth walls (see Mortensen et al. (2008); Marchioli et al. (2010), Marchioli and Soldati (2013) and Michel and Arcen (2021) among others). In these works, gravity was neglected to examine particle-turbulence interactions in isolation from other effects. In our work, this choice is motivated by the objective of evaluate the interplay between the large-scale roughness of the walls and the inertia of the particles in isolation from other effects that would affect directly on particle wall-normal transport (deposition at the bottom wall in the case of gravity). Nevertheless, the impact of gravitational settling represents one of the possible future developments of this work. We expect a quantitative effect on the particle velocity and concentration statistics, in a way that should strongly depend on the particle shape, as suggested by the recent studies of Challabotla et al. (2016) and Arcen et al. (2017). These Authors investigated gravity effects on the dynamical behavior of inertial fibers suspended in a turbulent flow inside a vertically-oriented channel. Challabotla et al. (2016) were able to show that the preferential clustering of fibers in near-wall low-speed streaks was unaffected by gravity. Overall gravity turned out to have negligible effects on some of the statistics of the least inertial fibers whereas the inclusion of gravity had a strong impact for heavier fibers. Arcen et al. (2017) demonstrated that gravity may induce a significant mean relative velocity between the dispersed phase and the continuous phase, which in turn greatly modifies the dynamics of non-spherical particles. Indeed, these Authors observed that the dynamics of ellipsoids is close to that of spheres without gravity, whereas it becomes strongly dependent on the particle shape with gravity.

3. Computational domain and simulation parameters

The flow domain consists of a channel bounded by two solid walls. Four different configurations were simulated: The first is the channel with smooth walls, and the other three refer to the case of channel bounded by rough walls with increasing roughness amplitude. Table 1 shows the geometric features of the computational domain for all configurations: the domain size along the streamwise (x_1), spanwise (x_2) and wall-normal (x_3) directions, the number of grid points used to discretize the domain and the corresponding mesh spacings. For the smooth channel (case F1), the size of the computational domain is set to $2\pi\delta\times\pi\delta\times2\delta$ in the streamwise, spanwise and wall-normal directions, respectively, with δ the half width of the channel. The domain length in the streamwise direction was duplicated for the rough cases (cases R1, R2 and R3).

Periodic boundary conditions are imposed in the streamwise and spanwise directions, while the no-slip condition is enforced at the walls. The cell spacing is uniform in the streamwise and spanwise directions, with grid size equal to $\Delta x_1^+ \approx 7$ and $\Delta x_2^+ \approx 4$, respectively. In the wall-normal direction, grid points are clustered in the near-wall region such that the distance between the solid wall and the nearest computational node is much lower than one wall unit. With rough walls, a curvilinear structured boundary-fitted grid is used to discretize the computational domain and accurately resolve the wall region. Furthermore, since wall roughness reduces the typical size of the turbulent structures when compared to the smooth-wall case, a very fine grid is used. As shown in Table 1, the first grid point along the wall-normal direction is closer to the rough wall ($\Delta x_{3,max}^+ = 0.048$) with respect to the flat wall ($\Delta x_{3,max}^+ = 0.096$). The specific mesh resolution and grid spacing in wall normal direction was chosen, exploiting a careful grid sensitivity analysis, to ensure a mesh-independent solution of the governing equation.

For the cases with rough walls, roughness shapes are modeled by superimposition of n sinusoidal functions (Napoli et al., 2008):

$$k(x_1) = \sum_{i=1}^{n} A_i \sin\left(\frac{2\,i\,\pi\,x_1}{L/2}\right) , \tag{9}$$

where $k(x_1)$ is the wall boundary distance from the horizontal reference surface, n is the number of sinusoidal functions, A_i is the amplitude and $L/2i$ is the wavelength of the ith function. For a more detailed description of the computational grid, the reader is referred to Milici et al. (2014). In this study, $n = 4$ and the sum of the sinusoidal functions is then subsequently scaled to obtain three distinct rough surfaces with averaged absolute deviation $\bar{k}$ equal to 0.012δ, 0.024δ and 0.050δ. The averaged absolute deviation is calculated as:

$$\bar{k} = \frac{1}{\delta}\frac{1}{L}\int_L |k(x_1)|\, dx_1 . \tag{10}$$

This way, the upper and lower walls have a different geometry locally but are equivalent in terms of roughness properties. The geometry of the solid walls is extruded along the spanwise direction, implying that wall roughness is two dimensional. The rationale behind the choice of considering a 2D roughness is the possibility to perform a direct comparison of our findings with those obtained previously for spherical particles on the same type of roughness (see, for instance, De Marchis et al. (2016). The analysis of fiber interaction with a fully three-dimensional roughness would be very interesting, of course, albeit complicated to handle and computationally costly in the presence of large swarms of fibers. As demonstrated by De Marchis and Napoli (2012) and De Marchis et al. (2015), a three-dimensional roughness has a significant influence on the energy dissipation, which in turn is expected to affect the transport of the fibers and their spatial distribution within the flow. Numerical simulations are currently under way to examine the effect of fully-3D rough walls over fiber distribution.

Table 2 summarizes the characteristic parameters of the rough walls considered in present work: the average absolute deviation of the roughness heights, $\bar{k}$, the equivalent sand-grain roughness, k_s, the highest roughness peaks, k_{max}, and the Effective Slope of roughness, ES. The geometric and physical properties of the elongated particles are reported in Table 3. In particular, we examined particles with a cross section of radius $a^+ = 0.36$, Stokes number $St^+ = 5$ and aspect ratios $\lambda = 1$ (spherical particles), 3 and 10. For the largest aspect ratio, the length of the particle is $l^+ = 2a^+\lambda = 7.2 \simeq 3.5\eta_{K,min}^+$ with $\eta_{K,min}^+$ the smallest value of the Kolmogorov length scale in the channel. The quantity b^+ is the dimensionless semi-major axis of the ellipsoid in wall units, whereas b is the dimensional value of the axis. The following relationship holds: $b = b^+/(u^*/\nu) = b^+/(Re_\tau/\delta)$.

According to Ravnik et al. (2018), the maximum root mean square error that may be incurred in the calculation of the Jeffery torques in

Table 3
Particle parameters: St^+ is the Stokes number; λ is the aspect ratio; S is the ratio of particle density ρ_p to fluid density; $2b^+$ and $2b$ are the ellipsoid's major axis in wall units and in dimensional units, respectively.

Set	St^+	λ	S	ρ_p [kg/m^3]	$2b^+$	$2b$ [μm]
P1	5	1	173.60	225.68	0.72	96.07
P3	5	3	92.90	120.77	2.16	287.93
P10	5	10	57.70	75.01	7.20	960.70

the present simulations is:

$$\|\mathbf{M}_J^a - \mathbf{M}_J^c\| \approx 0.041 \ \left(St^+\right)^{-0.34} \left(\frac{l^+}{\eta_K^+}\right)^{1.44} = 0.144 \ , \tag{11}$$

which is deemed acceptable for the purpose of examining trends in the particle behavior.

To ensure converged statistics, swarms of 200.000 fibers are tracked for each class, assuming dilute flow and hence one-way coupling between the phases. Particles were initially injected with random spatial distribution and random orientation over the entire computational domain. The initial velocity of the particles was set equal to the velocity of the fluid at the center of mass of the particle. In terms of boundary conditions, particles moving outside of the computational domain in the streamwise and/or spanwise directions were reintroduced via periodicity. The interaction between the particles and the solid walls were modeled considering purely elastic rebounds, which occur when the distance between the particle and the wall is less than semi-minor axis of ellipsoid. In the presence of rough walls, the elastic rebounds is clearly quite complex due to local variation of the boundary concavity, and to the specific trajectory of the particle. In order to overcome this issue, in the present study the collision detection algorithm proposed by De Marchis et al. (2016) was used, taking into account for the identification of the collision plane as well as the local concavity of the wall. The rebound algorithm was tested both using a simplified rebound model, used in the present research, and a modified rebound procedure, which takes into account the projection of the semi-major axis of the ellipsoid along the wall-normal direction to detect a particle–wall collision. The tests made (not shown here for sake of brevity) indicate that the steady-state fiber concentration is only marginally affected by either version of the rebound model. This minor impact of the rebound criterion is directly related to the effect that the large-scale roughness has on the wall-normal particle distribution.

The Panormus solver, as previously mentioned, is second order accurate both in time and space. To ensure the accuracy of the simulation, the rms velocity profiles as well as vorticity rms were compared, showing the ability of the solver to compute the velocity gradients with suitable accuracy. In Fig. 3, the streamwise and wall-normal turbulence intensities (panels (a) and (b), respectively) are compared with those reported by Marchioli et al. (2008) and Marchioli and Soldati (2013) using different Eulerian and Lagrangian solvers. In Fig. 3(c), the rms vorticity fluctuations are shown, whereas a comparison of the mean streamwise direction cosines, $cos|\theta_{x_1}|$, with those reported by Marchioli et al. (2010) is shown in Fig. 4. The comparison between Panormus solver and the results obtained by Marchioli et al. (2008) and Marchioli and Soldati (2013) at the same shear Reynolds number using a pseudo-spectral code shows an almost perfect overlap, thus ensuring the quality of the numerical simulations. The slight underestimation between our results and those reported by Mortensen et al. (2008) and Kim et al. (1987) is attributed to the higher Reynolds number of those simulations ($Re_\tau = 180$).

As a final remark of this Section, it should be noted that our results apply to dilute dispersions of sub-Kolmogorov particles. Therefore direct comparison with particle-resolved simulations available in the literature is not straightforward in view of the several differences in terms of flow configuration, simulation parameters (particle size, in particular) and assumptions made to perform the calculations. Consider the recent study of Jain et al. (2021), for instance. While we examine a closed channel bounded by two walls, these Authors considered an open channel flow. In addition, the particle-to-fluid density ratio is of the order of unity in Jain et al. (2021), which is roughly two orders of magnitude lower than in our study. The different specific density, in particular, has an impact on the hydrodynamic forces that determine the motion of the particles: For instance, the added mass force may be safely neglected in our problem (Soldati and Marchioli, 2009). Other differences are relative to the diluteness of the suspension (we consider mass and volume fractions that fall in the dilute regime, thus allowing us to neglect momentum coupling between the phases and inter-particle collisions; Jain et al. (2021) account for particle–particle collisions, as these are crucial to accurately simulate the bedload dynamics), the present of gravitational settling (which we neglect) and the specific geometrical features of the bottom roughness: In Jain et al. (2021), the bottom bed is made of several layers of densely-packed, coarse-grained particles.

4. Results

In the next sections, we discuss the effect of both roughness and aspect ratio on particle dynamics, specifically focusing on the instantaneous particle number density distribution (referred to as concentration hereinafter) and on the particle velocity and orientation statistics. These observables are provided for each value of the aspect ratio (to compare elongated particles with spherical ones) and for each value of roughness (to compare rough walls with smooth ones). Unless otherwise stated, the statistical quantities presented in this Section were calculated over a time-window of $t^+ = 10^5$ non-dimensional time units, which was verified to be long enough to ensure statistical convergence.

4.1. Particle distribution

Figs. 5 and 6 show the instantaneous spatial distribution of the particles as seen from a longitudinal section ($x_1 - x_3$ plane) and from a horizontal section ($x_1 - x_2$ plane) in the near-wall region close to the bottom wall, respectively. Let us focus first on Fig. 5(a), which refers to the smooth channel case (case F1) and also shows the streamwise velocity distribution in the selected monitor $x_1 - x_3$ plane taken at $x_2^+ = 100$. Only particles belonging to set P1 and located within the slice $\Delta_{x_2}^+ = 100 \pm 15$ are considered in this Figure. Particle are colored according to their vertical velocity: black (resp. white) particles move upwards (resp. downwards) in the vertical direction. Looking at the Eulerian fluid, Fig. 5 shows from a qualitative viewpoint a significant reduction of the average streamwise velocity component as walls become more rough. As demonstrated, among other by De Marchis (2012), the roughness effect manifests itself as a reduction of the mean velocity profile, known as Roughness function ΔU^+ and, as observed by Luo et al. (2019), the presence of wall-roughness reduces the streamwise particle velocity and increases the fluctuating velocities. This behavior is ruled by the tendency toward isotropization induced by the wall irregularities with a subsequent redistribution of the turbulent kinetic energy. This can be argue looking at the redistribution of the rms of the velocity fluctuations. Indeed, the roughness causes a reduction of the streamwise component of the turbulence intensities and an increase of the spanwise and wall-normal components (see among others De Marchis and Napoli (2012)). Focusing the attention on the Lagrangian particles, Fig. 5 reveals that these attain an inhomogeneous distribution throughout the channel and accumulate at both walls. Clusters of upward-moving particles and downward-moving particles alternate along the streamwise direction. A similar situation is observed in Fig. 5(b), which refers to the case with lowest roughness (case R1). Only particles belonging to set P1 and located within the slice $\Delta_{x_2}^+ = 100 \pm 30$ (chosen to display approximately a comparable subset of particles) are considered. From a qualitative

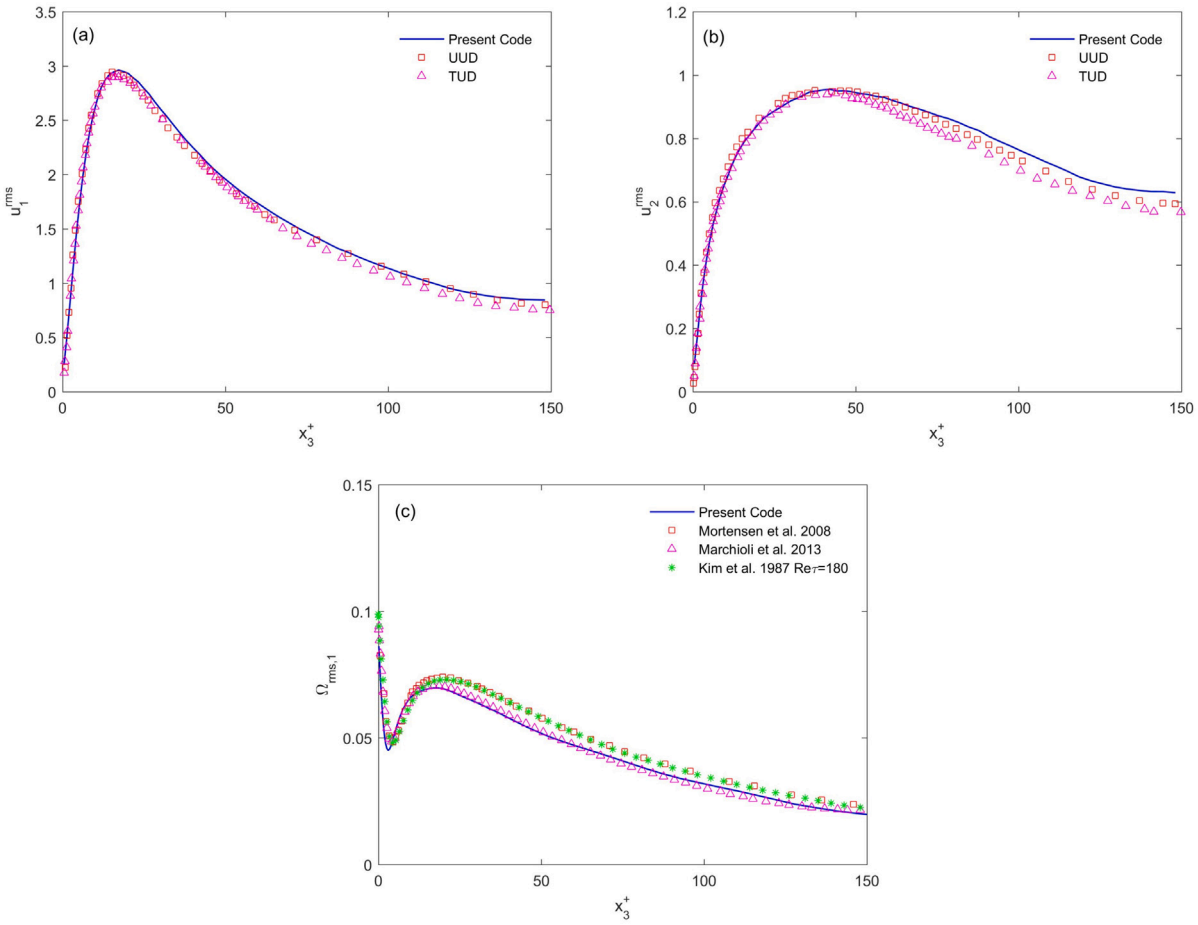

Fig. 3. Upper panels: Comparison of the fluid velocity rms (root mean square): (a) streamwise component, (b) spanwise component. Labels: UUD Group (results from Udine University), TUD Group (results from TU Delft). See Marchioli et al. (2008) for additional details about the UUD and TUD solvers. Lower panel (c): Comparison of the vorticity fluctuation rms in the streamwise direction and the results of Marchioli and Soldati (2013), Mortensen et al. (2008) and Kim et al. (1987).

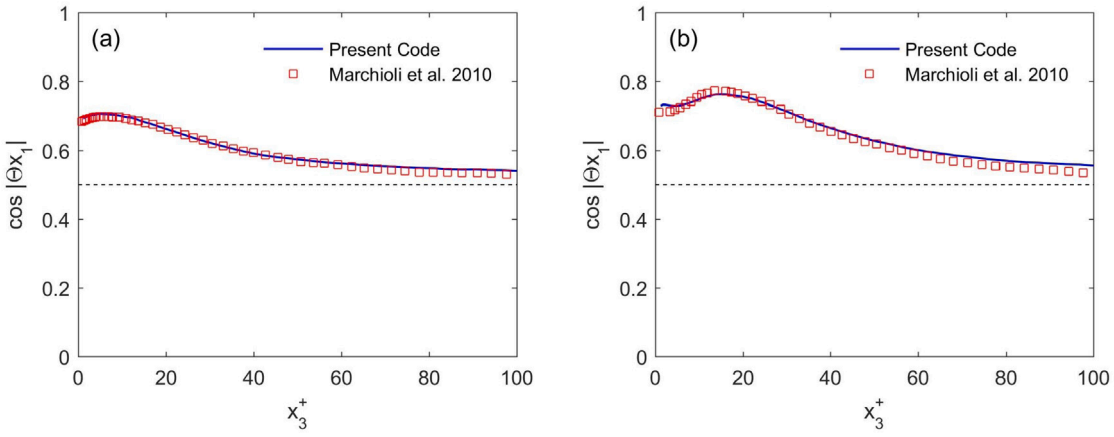

Fig. 4. Comparison of the mean streamwise direction cosines, $cos|\theta_{x_1}|$, with the results reported by Marchioli et al. (2010). Panels: (a) $\lambda = 3$ and (b) $\lambda = 10$.

standpoint, clusters and voids appear unaltered and wall accumulation is clearly visible. However, when roughness is further increased, as shown in Fig. 5(c) and (d) for the same particle set and fluid slice of Fig. 5(b), fewer particles are found in the near-wall region and a more uniform distribution of particles across the channel is attained. This trend was also observed in previous simulations of rough channel laden with spherical particles at similar Re_τ (Milici et al., 2014), and can be explained considering the behavior of the particles in the proximity of the rough wall: Particles move in the wall region following the shape of the roughness until they reach one of the highest peaks, where they are pushed back towards the channel center by the locally-high velocity gradients and bursting motions that can be originated near such peaks. The upward and downward motion of the particles are associated to their interaction with the flow produced by the roughness peaks. As demonstrated by De Marchis et al. (2010), the peaks of wall roughness induce the formation of shear layers directed diagonally toward the outer region. Particles are thus injected toward the outer region when interact with this shear layer. This type of fluid–particle interaction

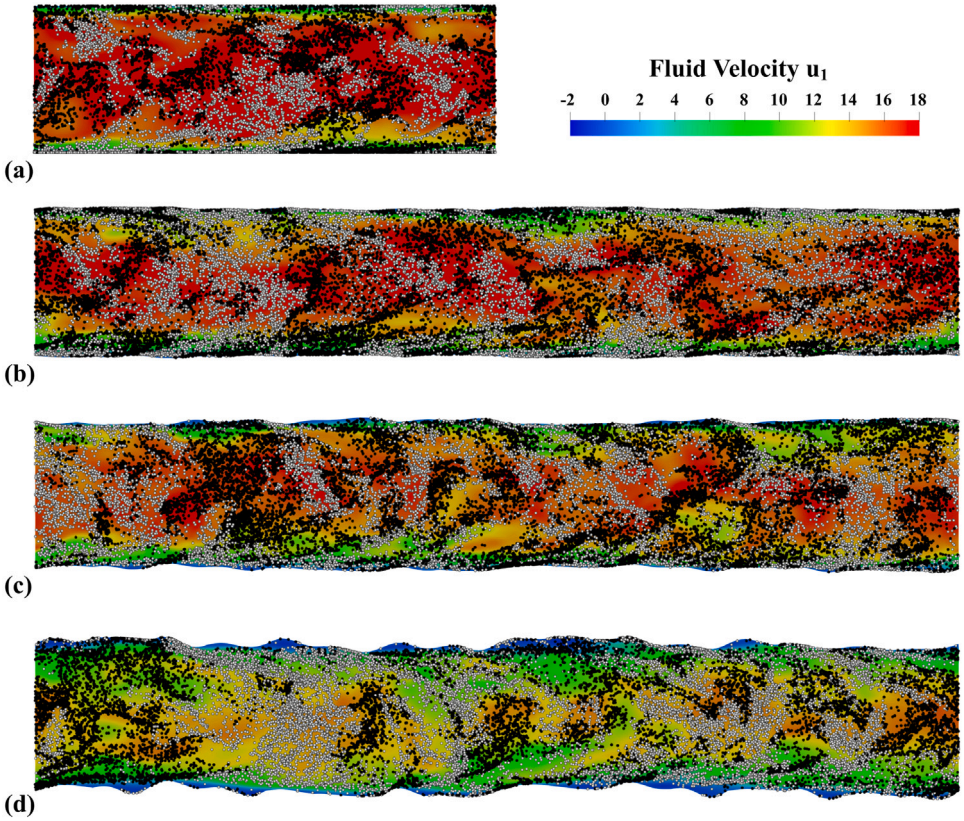

Fig. 5. Longitudinal $x_1 - x_3$ slice of the instantaneous particle distribution (set P1): black particles move upwards in the vertical direction, white particles move downward in the vertical direction. Also shown is the streamwise velocity component (the non-dimensional instantaneous values are provided by the color-bar). Panels: (a) Case F1, (b) Case R1, (c) Case R2 and (d) Case R3. (For interpretation of the references to color in this figure legend, the reader is referred to the web version of this article.)

prevents strong particle trapping in the cavities of the wall, where local recirculation bubbles may form. The effect becomes more and more evident as the mean height of the roughness is increased. Fig. 6 shows the instantaneous distribution of the particles in connection with the local height of the bottom rough wall along the streamwise direction: The highest positive peaks (measured with respect to the zero-level located at $x_3 = 0$) are colored in red, whereas the lowest negative peaks are colored in blue. Case R3 is taken here as reference and only particles located within a distance of 30 wall units from the wall are visualized. Particle color code is the same as in Fig. 5 (black particles are moving upward, white particles are moving downward).

In the case of smooth walls, particles in the near-wall region tend to sample the low-speed fluid streaks and, hence, form elongated clusters (Marchioli and Soldati, 2002). In the case of rough walls, our results indicate that this preferential sampling is blurred. The reason is that the peaks of roughness may destroy the fluid coherent structures that are responsible for the streaky structure of the fluid velocity field near the wall (De Marchis et al., 2010). In turn, this leads to a modification of particle distribution (Milici and De Marchis, 2016). Comparing the different panels of Fig. 6, which refer to the different particle sets considered in the simulations, it is apparent that the effect of the aspect ratio is minor since the position occupied by the clusters is nearly the same in all panels. Indeed, particle segregation into low-speed streaks is mainly driven by particle inertia, as discussed in Marchioli et al. (2010). Note that a higher number of black particles (moving upwards) appears to be located in the regions characterized by positive slope of roughness: it is precisely in these regions that particles can be re-entrained towards the bulk of the channel by the local bursting motions of the fluid, which increase wall-normal transport of mass and momentum and are associated with a reduction of streamwise fluid velocity.

4.2. Velocity statistics

Figs. 5 and 6 provide a qualitative representation of the flow and particle dynamics. The aim of the present study, however, is to characterize these dynamics from a statistical point of view. In this section, we thus start such characterization by looking at the particle velocity statistics. Fig. 7 shows the Eulerian velocity statistics, obtained for all flow configurations, and the Lagrangian (particle) velocity statistics, obtained for all particle sets. More specifically, Fig. 7(a) shows the mean streamwise fluid velocity profile in the wall normal direction (angle brackets $\langle\cdot\rangle$ indicate average in time, in the planes of statistical homogeneity $x_1 - x_2$ and considering symmetry with respect to the mid-plane): the solid line corresponds to the flat-wall case, while symbols are used for the different rough-wall cases. Profiles tend to overlap in the logarithmic region, suggesting that the mean velocity profile is not affected by roughness in this region. However, an increase of the averaged absolute deviation of roughness height leads to a decrease of the streamwise fluid velocity, especially in the core of the flow (as visible in Fig. 5 too). This decrease is associated with a near-wall decrease of the velocity defect law, which is calculated as the difference between the centerline velocity U_{cl}^+ and the fluid velocity u_i^+ at distance x_3/δ from the wall and is shown in Fig. 7(b). Profiles overlap in the outer region, thus supporting the validity of the similarity hypothesis (Townsend, 1976). Fig. 7(c) and (d) show the root mean square (rms) of the fluid and particles velocities, for the smooth-wall case F1 and for the rough-wall case R3, respectively. The streamwise rms profiles for the particles (symbols) differ from that of the fluid (solid line) regardless of the wall geometry: In the near-wall region, the particle rms always exhibits a higher peak compared to the fluid rms. Only with rough walls, the particle rms profile differ significantly from that of the fluid in the spanwise and wall-normal

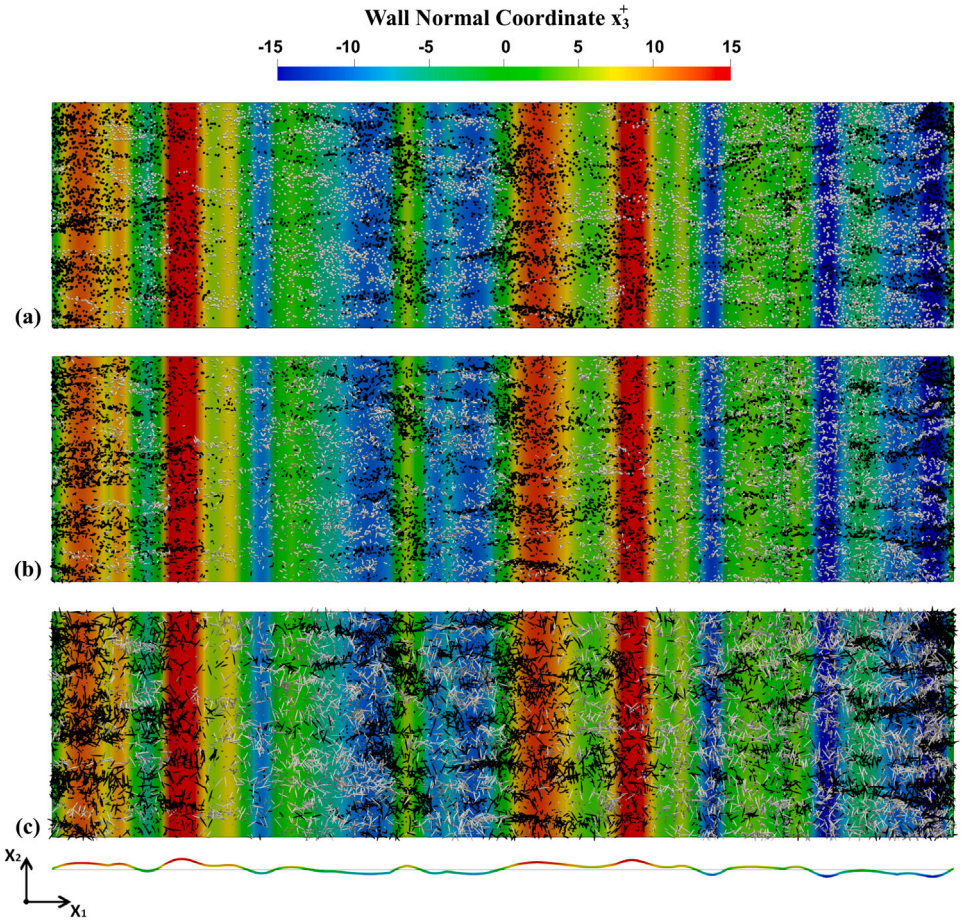

Fig. 6. Horizontal $x_1 - x_2$ slice of the instantaneous particle distribution for Case R3 (colors highlight the local height of the bottom rough wall). Only particles located within a distance $x_3^+ < 30$ from the bottom wall are shown. Particle color code is as in Fig. 5. Panels: (a) $\lambda = 1$, (b) $\lambda = 3$ and (c) $\lambda = 10$. (For interpretation of the references to color in this figure legend, the reader is referred to the web version of this article.)

directions. Note that, because of the one-way coupling assumption, all particle rms profiles nearly coincide indicating that the different aspect ratio does not play a role and particle fluctuating velocities depend almost exclusively on particle inertia. The results presented here are in agreement with the findings of Milici and De Marchis (2016), where the same Eulerian solver but different Lagrangian tracker was used and where the same computational domain and physical parameters are studied. On the other hand, the particle rms behavior shows some discrepancies with respect to that shown in Ji et al. (2013) and in Ji et al. (2014), resulting in a higher peak of the particle streamwise rms with respect to that of the fluid, but slightly lower peaks in the spanwise and wall-normal directions. In these latter studies, the entrainment and movement of coarse particles on the bed of an open channel is numerically investigated, treating the sediment as individual particles and investigates the interaction between turbulent coherent structures and particle entrainment. The difference can be attributed to the different modeling approach used to treat the particles. In our simulations, the particles are considered as pointwise and the gravity is neglected. Conversely, the above mentioned literature studies considered particles as finite size objects immersed in the fluid and the gravity is considered. Finally, additional differences are relative to the diluteness of the suspension we consider mass and volume fractions that fall in the dilute regime, thus allowing us to neglect momentum coupling between the phases and inter-particle collisions; conversely, Ji et al. (2013) and Ji et al. (2014) account for particle–particle collisions. Each of the aspects just mentioned may contribute in a non-trivial way to the fluid velocity seen by the particles and, in turn, to the particle velocity. Therefore, in the absence of a systematic study, it appears rather difficult to discern the relative importance of these aspects in determining the different distribution of the particle velocity fluctuations.

4.3. Concentration profiles and residence times

Particle concentration profiles for the different aspect ratios considered in this study are shown in Fig. 8. The profiles refer to the steady state condition for particle concentration, namely to a stage of the simulation for which the wall-normal volumetric number density of the particles, labeled as C hereinafter, does not change in time anymore (due to a balance of transfer fluxes to and away from the wall). The concentration profiles show the behavior of the number density, C, normalized by its initial value C_0, given by the ratio of the total number of particles tracked and the total volume of the flow domain Marchioli et al. (2010). Plots are truncated at $x_3^+ = 80$ because the trend observed in the region $40 < x_3^+ < 80$ persists throughout the channel center. An inset has been added in each panel of Fig. 8 to highlight concentration profiles near the wall when plotted with respect to a *virtual* origin of the wall-normal axis. Specifically, this virtual origin is set equal to the maximum roughness peak k_{max}^+ where the coordinate $x_3^+ - k_{max}^+$ is equal to zero in all rough-wall cases (De Marchis et al., 2010). By doing so, concentration profiles for a given particle set in the different flow configurations can be compared directly.

As well know, inertial particles dispersed in a turbulent channel flow tend to accumulate in the near-wall region (Marchioli and Soldati, 2002; De Marchis et al., 2010). Therefore, the peak of concentration

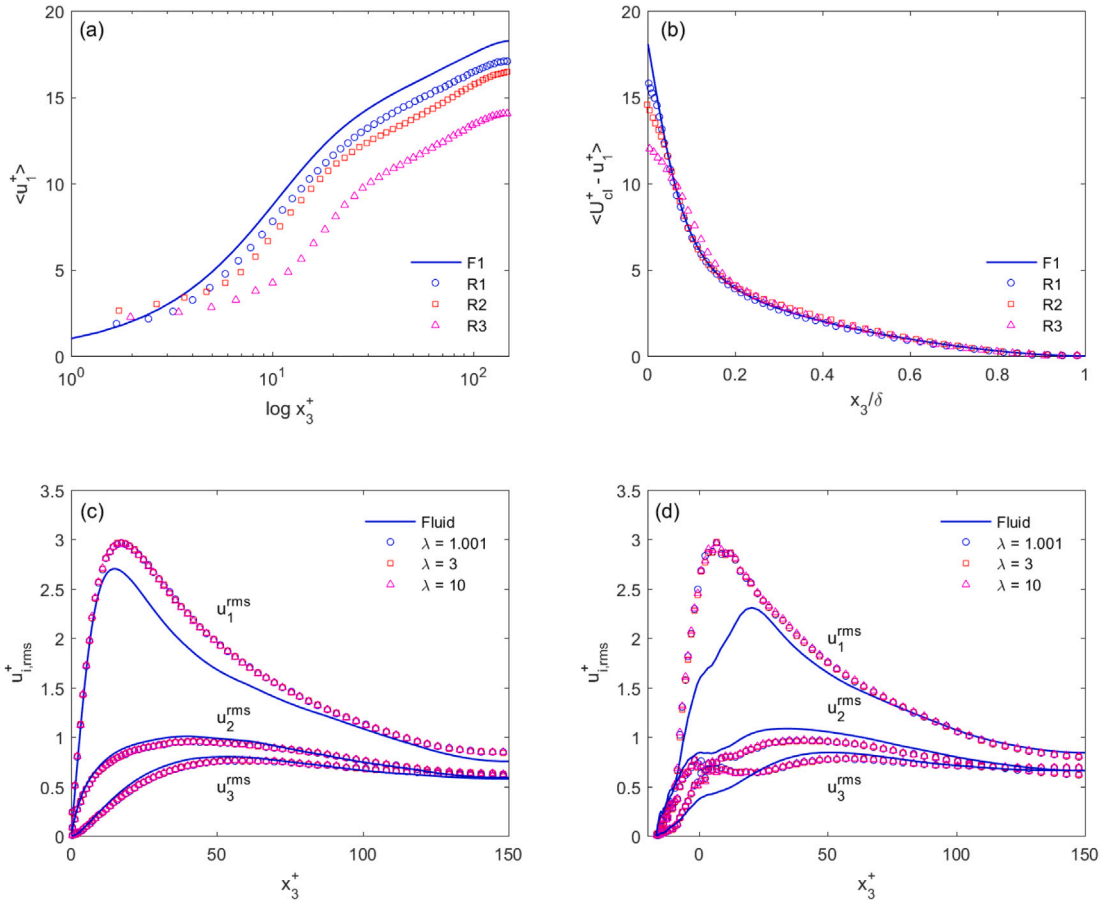

Fig. 7. Eulerian and Lagrangian velocity statistics, Panels: (a) Mean streamwise fluid velocity profiles, (b) Fluid velocity defect law profiles, (c) rms profiles for smooth walls case (F1), (d) rms profiles for high rough walls case (R3).

developed by the particles inside the viscous sublayer in the smooth-wall case (solid line in each panel) is well expected. Examination of the profiles for the rough-wall cases (R1, R2 and R3) shows that the near-wall peak of concentration decreases (ranging from $C/C_0 \approx 4.5$ in case R1 to $C/C_0 \approx 1.5$ in case R3) as the roughness is increased and its location shifts towards higher values of x_3^+, where the highest roughness peaks are found. Compared to the smooth-wall case, particles appear more uniformly distributed throughout the channel height. Note that concentration profiles collapse onto each other in the outer region of the flow when plotted as a function of the $x_3^+ - k_{max}^+$ coordinate (as clearly visible in the insets of Fig. 8). This hints to the role played by the roughness height in determining the particle distribution in the vertical direction. We also note an effect of the aspect ratio. For spherical particles (inset of Fig. 8(a), profiles evaluated with respect to the virtual origin always recover the concentration profile of the smooth-wall case up to the location of the peak (see Fig. 8(a) and inset) whereas they are systematically above the smooth-wall concentration for $\lambda = 3$ (see Fig. 8(b) and inset) and for $\lambda = 10$ (see Fig. 8(c) and inset). Note that, albeit the difference between the peaks observed for $\lambda = 3$ and $\lambda = 10$ is very slight, we do find the highest concentration peak for $\lambda = 3$. This suggests that lower concentration peaks might be expected for aspect ratios larger than 10.

As a final remark, we note that the peaks of particle concentration at or very near the smooth wall are consistently much higher than those observed in numerical simulations of flexible fibers in closed channel flow (Dotto and Marchioli, 2019; Dotto et al., 2019) and in experimental measurements made for rigid, yet curved, fibers in open channel flow (Alipour et al., 2021). The reasons for such differences are not straightforward to explain and, in our opinion, deserve future investigations to verify whether they can be ascribed to limited modeling capabilities of the pointwise Lagrangian approach for non-spherical particles.

To quantify the particle ability to stay in the viscous region, we now examine the PDF of particle residence time in the viscous sublayer ($x_3^+ < 5$), shown in Fig. 9. The residence time of each particle is defined here as the maximum time span between one entrance in the viscous sublayer and the following exit, up to a maximum span $T^+ = 100$ (namely, a particle is given a residence time equal to T^+ even if it stays longer in the viscous sublayer: this choice was made for visualization purposes). To compute the PDF, we divided the span T^+ into 100 sub-intervals t_i^+ and, for each sub-interval, we counted the number of particles N_i with a residence time falling within t_i^+. Finally, we normalized N_i by the total number of particles tracked. The PDFs so obtained are shown in Fig. 9 at varying aspect ratio for the different wall geometries. Each panel refers to a specific value of the aspect ratio, and the inset shows the behavior of the PDF for short residence times (lower than $t^+ = 30$).

First of all, let us discuss the peak of the PDFs at $t^+ = 100$. The range of residence times measured in our simulations is very wide and extends to values much larger than T^+. Therefore, the peak simply indicates that a significant number of particles is able to remain inside the viscous sublayer for very long times. This is especially true in the smooth-wall case (solid line). However, the $t^+ = 100$ peak systematically decreases as roughness increases. In particular, the decrease is significant in the two cases R1 (circles) and R2 (squares) and tends to saturate in case R3 (triangles). In fact, for particles with $\lambda = 3$,

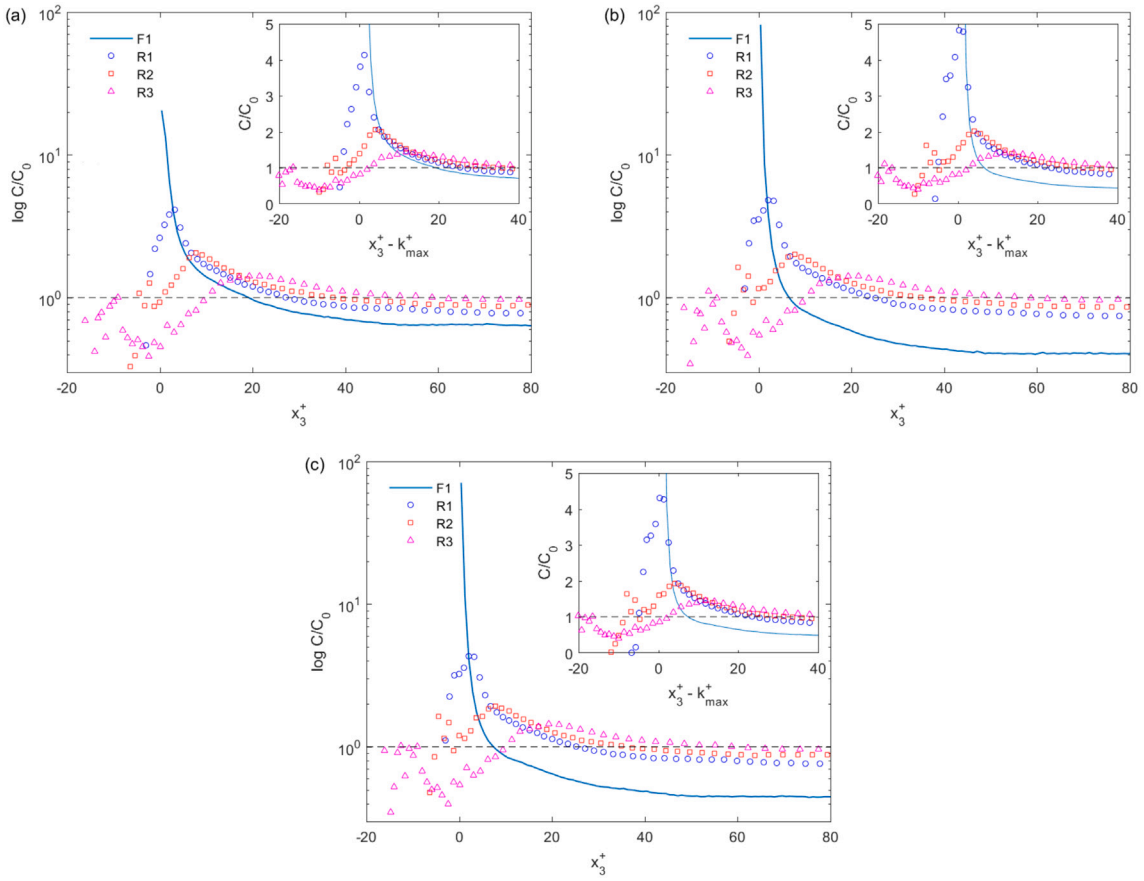

Fig. 8. Wall-normal concentration profiles in the different flow configurations (the solid line refers to the smooth-wall case F1, symbols refer to the different rough-wall cases). Panels: (a) $\lambda = 1$, (b) $\lambda = 3$ and (c) $\lambda = 10$. Each inset provides a close-up view of the profiles in the near-wall fluid slab $x_3^+ < 40$ of $C/C0$ vs $x_3^+ - k_{max}$.

Fig. 9(b), and $\lambda = 10$, Fig. 9(c), almost no peak reduction is observed between case R2 and case R3. The peak of the PDFs, at residence times approximately equivalent to the particle Stokes number, is associated with particles that are brought to the wall by a coherent in-sweep fluid motion generated by a near-wall vortex. Once in the viscous sublayer, particles are able to escape by following the fluid ejection that the same vortex generates. As shown by Soldati and Marchioli (2009), the characteristic timescale of the turbulent vortical structures in the near-wall region, given in terms of local dimensionless eddy turnover, scales linearly with the wall-normal coordinate within the viscous sublayer (while decreasing progressively as the structures lie closer to the wall). This implies that the vortical structures that govern particle transport to and away from the wall have a characteristic timescale of the order of the particle Stokes number. Therefore, a short residence time indicates that a particle penetrating the viscous sublayer may exit by being transported on the same vortical structure which brought it inside in the first place. Particles that are not able to follow the same vortical structure are bound to remain trapped inside the viscous sublayer for much longer times. This type of behavior is driven mainly by particle inertia and, because of this, can be observed also in the case of channel flow within smooth walls, as discussed in Soldati and Marchioli (2009).

The effect of roughness is also visible in the lower end of the residence times interval, namely for $t^+ < 15 \div 20$. An increase of roughness is systematically associated with an increase of the PDF, which develops a peak around $t^+ \simeq 5 = St^+$. No clear peak can be detected in the smooth-wall case. Overall, these findings indicate that particles in the proximity of a rough wall are less likely to be trapped inside the viscous sublayer for very long times and a fraction of them tends to leave this region after a short time interval scaling with the Stokes number, namely with particle inertia. Again, very little dependence of the PDF on the aspect ratio is observed.

4.4. Orientation statistics

In the previous sections, the effect of roughness on the statistical observables examined was evident, and appeared to overcome any possible effect due to a change in the shape (aspect ratio) of the particle. This shape-independence of statistics may be ascribed to the fact that they were mostly related to the translational motion of the particles rather than to their rotational motion. To verify if shape effects become comparable to roughness effects when statistics stemming from particle rotation are considered, we now turn our attention to two different types of orientation statistics: The absolute values of mean direction cosines and the orientation frequency in the near-wall region ($x_3^+ < 10$). To compute particle orientation, the angles Θ_{x_i} formed by the major x_3' axis of the particle with respect to the axes of co-moving frame $\langle x_1'', x_2'', x_3'' \rangle$, as shown in Fig. 10. According to this definition, a particle is aligned to a specific direction, x_i, if $\cos|\Theta x_i| = 1$. The resulting direction cosines are plotted, as a function of the wall normal coordinate, in Fig. 11. The left-end panels, labeled (a), (d) and (g), show the direction cosines for the smooth-wall case F1; the panels in the middle column, labeled (b), (e) and (h), show the direction cosines for the rough-wall case R1; the panels in the right-end column, labeled (c), (f) and (i), show the direction cosines for the rough-wall case R3. The horizontal axis is truncated at $x_3^+ = 100$ because farther from the wall all the profiles collapse to the value $\cos|\Theta x_i| \approx 0.5$, which corresponds to a uniform distribution of particle orientations in the 3D space. The effect of roughness can be appreciated comparing panels on the same

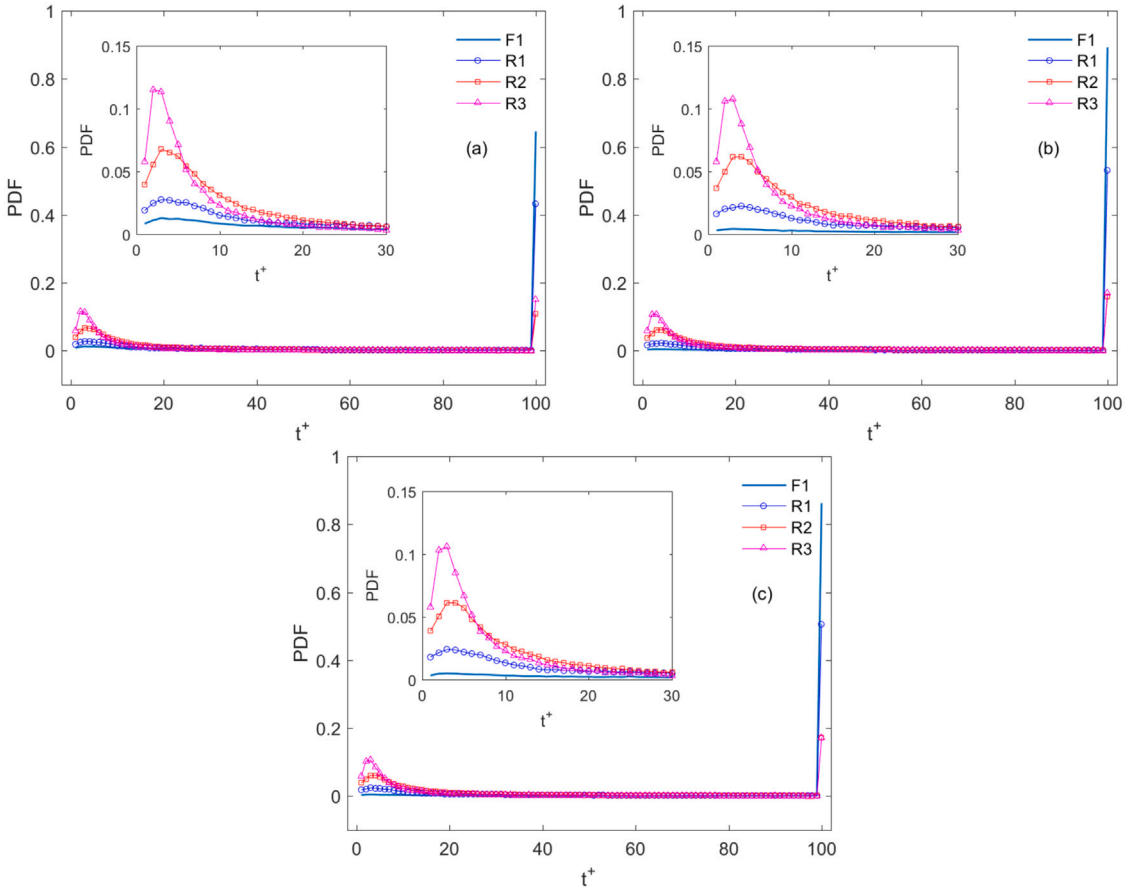

Fig. 9. PDF of residence time of particles in the viscous sublayer. Panels: (a) $\lambda = 1$, (b) $\lambda = 3$ and (c) $\lambda = 10$. The inset in each panel provides a close-up view of the PDFs in the lower end of the residence times interval.

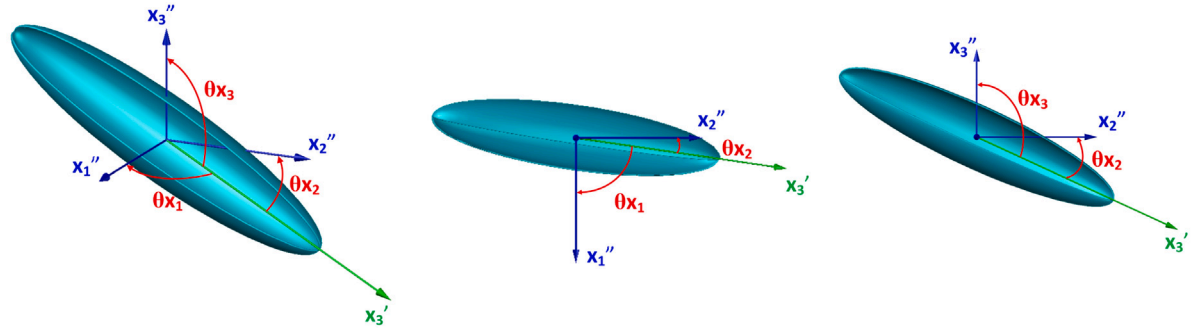

Fig. 10. Schematic representation of the angles Θ_i used to compute direction cosines.

row; the effect of the aspect ratio can be appreciated comparing the profiles plotted in the same panel.

As far as roughness effects are concerned, changes in the profile are generally more evident near the wall in case R3. The profile of the streamwise cosine $\cos|\Theta x_1|$ flattens for particles with $\lambda = 3$ (red squares) and $\lambda = 10$ (pink triangles), while being unaffected for spherical particles (blue circles). The spanwise cosine $\cos|\Theta x_2|$, which attains a minimum at the wall (for $\lambda = 10$) or very near to it (for $\lambda = 3$) as shown in Fig. 11(d), is characterized by a shift of such minimum away from the wall in case R1, Fig. 11(e), and by a change of slope in case R3, Fig. 11(f). This change produces a maximum value of $\cos|\Theta x_2|$ right at the wall for both $\lambda = 3$ and $\lambda = 10$. For the wall-normal cosine $\cos|\Theta x_3|$, the local peaks observed at the wall for $\lambda = 3$ and $\lambda = 10$ in the smooth-wall case, Fig. 11(g), are observed to shift away from the wall in case R1, Fig. 11(h), and are not occurring in case R3: In the latter case, both profiles end reaching a minimum value. Overall, the decrease of $\cos|\Theta x_1|$ to values close to 0.5, and of $\cos|\Theta x_3|$ to values closer to 0, combined with the increase of $\cos|\Theta x_2|$ to values close to 0.5 in the near-wall region, indicates that the main effect of roughness is to align particles with their major axis closer to the $x_1 - x_2$ plane, where they tend to orient more uniformly than in the presence of smooth walls.

As far as aspect ratio effects are concerned, significant modifications to the profiles are obtained for elongated particles compared to the spherical ones, which are characterized by uniform orientation $\cos|\Theta x_i| = 0.5$ regardless of the flow direction. In general, an elongated particle exhibits a stronger tendency to align with the streamwise direction and perpendicular to the spanwise direction as it approaches a smooth wall. Such preferential alignment, however, is partially randomized by roughness and only a partial geometry-induced alignment

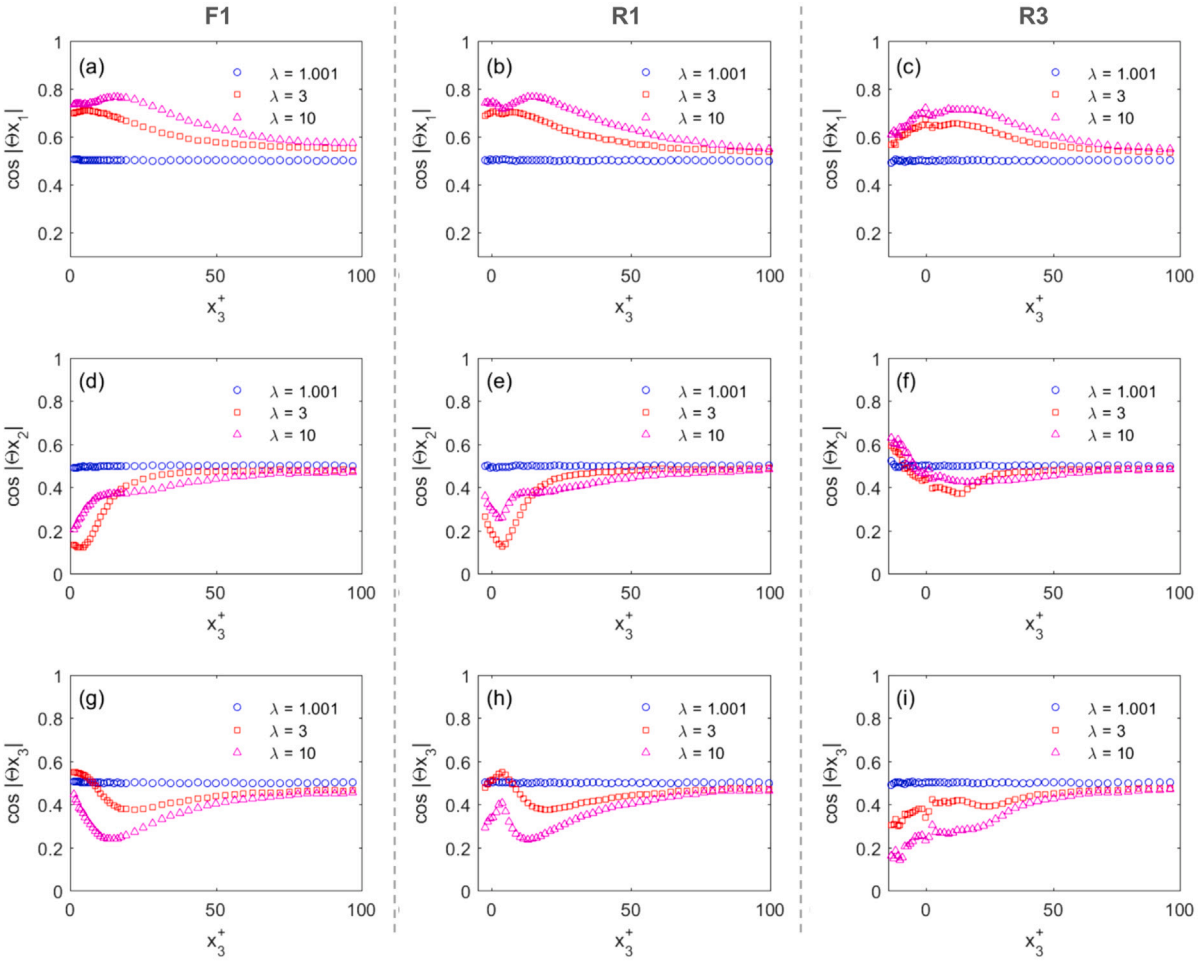

Fig. 11. Absolute values of the mean direction cosines. Panels: (a), (d), (g) Case F1; (b), (e) (h) Case R1; (c), (f), (i) Case R3.

with the wall persists. As could be expected, shape effects related to a change of aspect ratio do appear in orientation statistics, but appear to be quantitative rather than qualitative (i.e. different values of λ do not change the physical mechanism that governs particle rotation in the present simulation set-up).

The direction cosines were analyzed also by Marchioli et al. (2010) for the case of rigid ellipsoidal particles in turbulent channel flow with smooth walls. In that case, it was observed that the preferential near-wall alignment, though statistically probable, is quite unstable and can only be maintained for rather short times before the particles are forced to rotate around the spanwise axis by the shear-induced wall-normal velocity gradient. To verify if (and how) roughness can affect this instability, we follow Marchioli et al. (2010) and discuss next the near-wall particle orientation frequency, defined as the overall time spent by the particle in a given position of alignment with respect to the mean flow. The calculation procedure is the same of Marchioli et al. (2010), to which the reader is referred to for more details. Here, we just recall that particle alignment is classified by subdividing the absolute value of the direction cosines into k equally-spaced bins and by computing the overall time $t^+(i,j,k)$ spent by the ith particle belonging to the jth set in the kth bin. The mean time per bin $t^+(j,k)$ is then computed by averaging $t^+(i,j,k)$ over the number of particles per bin, and its percentage value is finally obtained as $\%t^+ = t^+(j,k)/T^+$. The outcome of this procedure is shown in Fig. 12 for particles in the near-wall region ($x_3^+ < 10$). For sake of brevity, only results for the streamwise direction cosine, in Fig. 12(a) and (b), and for the wall-normal direction cosine, in Fig. 12(c) and (d) are shown. Panels on the left-end column refer to the smooth-wall case F1, whereas panels on the right-end column refer to the rough-wall case R3. As expected, spherical particles have no preferential orientation, and their orientation frequency is $\%t^+ = 10$ in all cases. Focusing the attention on elongated particles, the effect of the aspect ratio is to increase the time spent with alignment in the streamwise direction, as shown in Fig. 12(a), where results confirm those reported in Marchioli et al. (2010), and in Fig. 12(b). At the same time, we observe an effect of the roughness that weakens this tendency: The orientation frequency associated with $\cos|\Theta x_1|$ in the alignment bin $[0.9 \div 1.0]$ decreases from $\%t^+ \approx 35$ to $\%t^+ \approx 20$ for particles with $\lambda = 3$ and from $\%t^+ \approx 42$ to $\%t^+ \approx 32$ for particles with $\lambda = 10$. Correspondingly, values of $\%t^+$ increase in the other bins. The combined effect of aspect ratio and roughness is visible also in Fig. 12(c) and (d), which refer to the orientation frequency associated with $\cos|\Theta x_3|$. In the smooth-wall case, Fig. 12(c), the aspect ratio produces a slight increase of $\%t^+$ in the alignment bin for the $\lambda = 3$ particles, and in the $[0 \div 0.1]$ bin for the $\lambda = 10$ particles. Albeit limited, these changes indicate a non-monotonic effect of λ on $\%t^+$ for the smooth-wall case, as also observed in Marchioli et al. (2010). However, with rough walls, as shown in Fig. 12(d), we find a systematic increase of $\%t^+$ in the $[0 \div 0.1]$ bin (this time monotonic with λ). In turn, the probability of finding particles aligned to the wall-normal direction becomes increasingly lower. In particular, particles with aspect ratio $\lambda = 10$ spend about 35% of their time in the region $x_3^+ < 10$ in the $[0 \div 0.1]$ bin and 85% of this time with $\cos|\Theta x_3| < 0.4$. This suggests a preferred seesaw-like rotation by the particles near the rough surface, characterized by alternate oscillations of their tips, as particles are advected downstream.

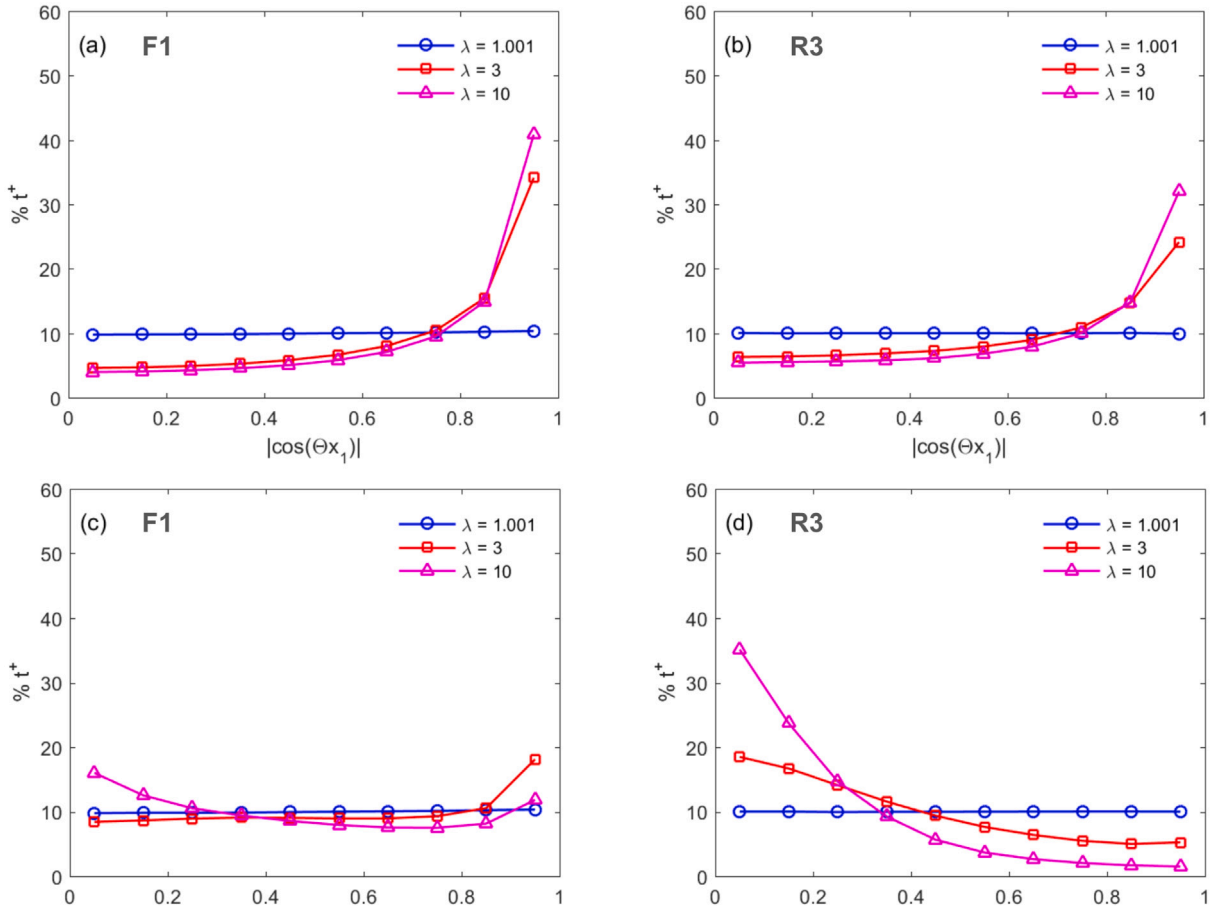

Fig. 12. Orientation frequencies (percent values) in the near-wall region ($x_3^+ < 10$). Panels: (a), (c) case F1; (b), (d) Case R3.

5. Final remarks

The dynamics of ellipsoidal particles dispersed in a turbulent channel flow bounded by rough walls was analyzed with Direct Numerical Simulations coupled with Lagrangian Particle Tracking. Particles with Stokes number $St^+ = 5$ and different aspect ratios were injected in a flow at $Re_\tau = 150$ and their trajectories were tracked assuming dilute flow conditions and one-way coupling with the carrier fluid. To examine the effect of roughness, the particle-laden flow in a channel bounded by two-dimensional rough walls characterized by three different amplitudes of the mean roughness height was compared to the classical channel flow within smooth walls. Three different sets of particles, classified by their aspect ratio $\lambda = 1$, 3 and 10, were considered to highlight differences in the behavior of the dispersed phase induced by changes in particle elongation. Our results show that particle distribution and translational statistics are practically unaffected by the aspect ratio and depend only on the specific wall geometry, which modifies the flow field in which particles are brought about. Instantaneous and averaged statistics obtained for the smooth-wall case show that particles accumulate in the viscous region, as previously demonstrated in several studies — see Soldati and Marchioli (2009) for a detailed review. The presence of rough walls, on the other hand, reduces considerably the net flux of particles that can be trapped in the near-wall region. This effect shows up clearly in the wall-normal concentration profiles, and depends monotonically of the averaged absolute deviation of the roughness $\bar{k}$. The PDF of the particle residence time in the viscous sublayer support this observation, since rough walls are found to decrease the residence time of all particle sets examined in this study.

The effect of roughness is found to combine with the effect of the aspect ratio in the statistics associated to particle orientation, especially for case R3 (highest roughness). The influence of roughness and aspect ratio on the absolute values of the mean direction cosines is concentrated in the near-wall region: The outer region of the flow is unaffected and profiles always collapse to the value (0.5) that corresponds to a uniform sampling of the three-dimensional orientation space. We also examined orientation frequencies, and found that elongated particles tend to align in the streamwise direction regardless of the wall geometry, but the percentage of aligned particles becomes smaller and smaller as the averaged absolute deviation of roughness is increased.

Future developments of this work include the analysis of a wider range of particle Stokes numbers and higher values of the flow Reynolds numbers, in order to evaluate the validity of the present findings at higher turbulence intensity. More dense suspension could also be considered, in order to evaluate the effect of two-way coupling between the phases and the effect of inter-particle collisions. Finally, the effect of the roughness on flexible elongated particles will be analyzed. The behavior of flexible particles, specifically fibers, has been examined recently by Dotto and Marchioli (2019) and by Dotto et al. (2019) for the case of turbulent channel flow within smooth walls. Considering the tendency of flexible particles to coil or stretch under the action of the turbulent velocity gradients, it would be interesting to evaluate the behavior of these particles in the cavities of the rough walls, and the resulting trapping dynamics.

CRediT authorship contribution statement

Domenico Saccone: Concept, Design, Analysis, Writing, or revision of the manuscript. **Cristian Marchioli:** Concept, Design, Analysis,

Writing, or revision of the manuscript. **Mauro De Marchis:** Concept, Design, Analysis, Writing, or revision of the manuscript.

Declaration of competing interest

The authors declare that they have no known competing financial interests or personal relationships that could have appeared to influence the work reported in this paper.

References

Alipour, M., De Paoli, M., Ghaemi, S., Soldati, A., 2021. Long non-axisymmetric fibres in turbulent channel flow. J. Fluid Mech. 916, A3. http://dx.doi.org/10.1017/jfm.2021.185.

Arcen, B., Ouchene, R., Khalij, M., Tanière, A., 2017. Prolate spheroidal particles' behavior in a vertical wall-bounded turbulent flow. Phys. Fluids 29 (9), 093301.

Balachandar, S., 2009. A scaling analysis for point-particle approaches to turbulent multiphase flows. Int. J. Multiph. Flow. 35 (9), 801–810.

Balachandar, S., Eaton, J.K., 2010. Turbulent dispersed multiphase flow. Annu. Rev. Fluid Mech. 42 (1), 111–133.

Benedini, M., 2020. Water pollution control. pp. 205–229.

Brandt, L., Schlatter, P., Casciola, C.M., 2011. Transport of inertial particles in turbulent boundary layers. J. Phys. Conf. Ser. (October 2016).

Brenner, H., 1963. The Stokes resistance of an arbitrary particle. Chem. Eng. Sci. 18 (1), 1–25.

Burns, P., Meiburg, E., 2015. Sediment-laden fresh water above salt water: nonlinear simulations. J. Fluid Mech. 762, 156–195. http://dx.doi.org/10.1017/jfm.2014.645.

Challabotla, N.R., Zhao, L., Andersson, H.I., 2016. Gravity effects on fiber dynamics in wall turbulence. Flow Turbul. Combust. 97 (4), 1095–1110.

Chandrappa, R., Das, D., 2021. Air pollution control. pp. 127–140. http://dx.doi.org/10.1007/978-3-030-64484-0_6.

Chen, Q., Xiong, T., Zhang, X., Jiang, P., 2020. Study of the hydraulic transport of non-spherical particles in a pipeline based on the CFD-dem. Eng. Appl. Comput. Fluid Mech. 14 (1), 53–69. http://dx.doi.org/10.1080/19942060.2019.1683075, eprint: https://doi.org/10.1080/19942060.2019.1683075.

Coleman, S.W., Vassilicos, J.C., 2009. A unified sweep-stick mechanism to explain particle clustering in two- and three-dimensional homogeneous, isotropic turbulence. Phys. Fluids 21 (11), 113301. http://dx.doi.org/10.1063/1.3257638.

Connolly, B.J., Loth, E., Smith, C.F., 2020. Shape and drag of irregular angular particles and test dust. Powder Technol. (ISSN: 0032-5910) 363, 275–285. http://dx.doi.org/10.1016/j.powtec.2019.12.045, URL: https://www.sciencedirect.com/science/article/pii/S0032591019311519.

Cui, Z., Dubey, A., Zhao, L., Mehlig, B., 2020. Alignment statistics of rods with the Lagrangian stretching direction in a channel flow. J. Fluid Mech. 901, A16. http://dx.doi.org/10.1017/jfm.2020.547.

Cui, Z., Huang, W., Xu, C., Andersson, H.I., Zhao, L., 2021. Alignment of slender fibers and thin disks induced by coherent structures of wall turbulence. Int. J. Multiph. Flow. (ISSN: 0301-9322) 145, 103837. http://dx.doi.org/10.1016/j.ijmultiphaseflow.2021.103837, URL: https://www.sciencedirect.com/science/article/pii/S0301932221002640.

D'Alessandro, G., Hantsis, Z., Marchioli, C., Piomelli, U., 2021. Accuracy of bed-load transport models in eddy-resolving simulations. Int. J. Multiph. Flow. (ISSN: 0301-9322) 141, 103676. http://dx.doi.org/10.1016/j.ijmultiphaseflow.2021.103676, URL: https://www.sciencedirect.com/science/article/pii/S0301932221001245.

De Marchis, M., 2012. Large eddy simulations of roughened channel flows: Estimation of the energy losses using the slope of the roughness. Comput. & Fluids 140, 148–157. http://dx.doi.org/10.1016/j.compfluid.2016.09.021.

De Marchis, M., Milici, B., 2016. Turbulence modulation by micro-particles in smooth and rough channels. Phys. Fluids 28 (11), 115101. http://dx.doi.org/10.1063/1.4966647.

De Marchis, M., Milici, B., Napoli, E., 2015. Numerical observations of turbulence structure modification in channel flow over 2D and 3D rough walls. Int. J. Heat Fluid Flow (ISSN: 0142-727X) 56, 108–123. http://dx.doi.org/10.1016/j.ijheatfluidflow.2015.07.002, URL: https://www.sciencedirect.com/science/article/pii/S0142727X15000843.

De Marchis, M., Milici, B., Napoli, E., 2017. Solid sediment transport in turbulent channel flow over irregular rough boundaries. Int. J. Heat Fluid Flow 65, 114–126.

De Marchis, M., Milici, B., Napoli, E., 2019. Large eddy simulations on the effect of the irregular roughness shape on turbulent channel flows. Int. J. Heat Fluid Flow 80, 117–131. http://dx.doi.org/10.1016/j.ijheatfluidflow.2019.108494.

De Marchis, M., Milici, B., Sardina, G., Napoli, E., 2016. Interaction between turbulent structures and particles in roughened channel. Int. J. Multiph. Flow. (ISSN: 0301-9322) 78, 117–131. http://dx.doi.org/10.1016/j.ijmultiphaseflow.2015.09.011, URL: https://www.sciencedirect.com/science/article/pii/S0301932215002098.

De Marchis, M., Napoli, E., 2012. Effects of irregular two-dimensional and three-dimensional surface roughness in turbulent channel flows. Int. J. Heat Fluid Flow (ISSN: 0142-727X) 36, 7–17.

De Marchis, M., Napoli, E., Armenio, V., 2010. Turbulence structures over irregular rough surfaces. J. Turbul. (11), 1–32.

De Marchis, M., Saccone, D., Milici, B., Napoli, E., 2020. Large eddy simulations of rough turbulent channel flows bounded by irregular roughness : Advances toward a universal roughness correlation. Flow Turbul. Combust. 105 (2), 627–648.

Dotto, D., Marchioli, C., 2019. Orientation, distribution, and deformation of inertial flexible fibers in turbulent channel flow. Acta Mech. 230 (2), 597–621. http://dx.doi.org/10.1007/s00707-018-2355-4.

Dotto, D., Soldati, A., Marchioli, C., 2019. Deformation of flexible fibers in turbulent channel flow. Meccanica 55 (2), 343–356. http://dx.doi.org/10.1007/s11012-019-01074-4.

Eaton, J.K., Fessler, J.R., 1994. Preferential concentration of particles by turbulence. Int. J. Multiph. Flow. 20, 169–209.

Fan, F.G., Ahmadi, G., 1995. A sublayer model for wall deposition of particles in turbulent streams. J. Aerosol Sci. 26 (5), 813–840.

Fong, K.O., Amili, O., Coletti, F., 2019. Velocity and spatial distribution of inertial particles in a turbulent channel flow. J. Fluid Mech. 872, 367–406. http://dx.doi.org/10.1017/jfm.2019.355.

Goto, S., Vassilicos, J.C., 2008. Sweep-stick mechanism of heavy particle clustering in fluid turbulence. Phys. Rev. Lett. 100, 054503. http://dx.doi.org/10.1103/PhysRevLett.100.054503, URL: https://link.aps.org/doi/10.1103/PhysRevLett.100.054503.

Jain, R., Tschisgale, S., Fröhlich, J., 2020. Effect of particle shape on bedload sediment transport in case of small particle loading. Meccanica 55, 299–315, URL: https://doi.org/10.1007/s11012-019-01064-6.

Jain, R., Tschisgale, S., Fröhlich, J., 2021. Impact of shape: DNS of sediment transport with non-spherical particles. J. Fluid Mech. 916, A38. http://dx.doi.org/10.1017/jfm.2021.214.

Jeffery, G.B., 1922. The motion of ellipsoidal particles immersed in a viscous fluid. Proc. R. Soc. Lond. Ser. A (102), 161.

Ji, C., Munjiza, A., Avital, E., Ma, J., Williams, J.J.R., 2013. Direct numerical simulation of sediment entrainment in turbulent channel flow. Phys. Fluids 25 (5), 056601. http://dx.doi.org/10.1063/1.4807075.

Ji, C., Munjiza, A., Avital, E., Xu, D., Williams, J.J.R., 2014. Saltation of particles in turbulent channel flow. Phys. Rev. E 89, 052202.

Kim, J., Moin, P., Moser, R., 1987. Turbulence statistics in fully developed channel flow at low Reynolds numbe. J. Fluid Mech.S 177, 133–166.

Lucci, F., Ferrante, A., Elghobashi, S., 2010. Modulation of isotropic turbulence by particles of Taylor length-scale size. IJournal of Fluid Mechanics 650, 5–55.

Lundell, F., Söderberg, L.D., Alfredsson, P.H., 2011. Fluid mechanics of papermaking. Annu. Rev. Fluid Mech. 43 (1), 195–217. http://dx.doi.org/10.1146/annurev-fluid-122109-160700.

Luo, K., Dai, Q., Liu, X., Fan, J., 2019. Effects of wall roughness on particle dynamics in a spatially developing turbulent boundary layer. Int. J. Multiph. Flow. (ISSN: 0301-9322) 111, 140–157.

Mallouppas, G., van Wachem, B., 2013. Large eddy simulations of turbulent particle-laden channel flow. Int. J. Multiph. Flow. (ISSN: 0301-9322) 54, 65–75. http://dx.doi.org/10.1016/j.ijmultiphaseflow.2013.02.007, URL: https://www.sciencedirect.com/science/article/pii/S0301932213000487.

Marchioli, C., Bhatia, H., Sardina, G., Brandt, L., Soldati, A., 2019. Role of large-scale advection and small-scale turbulence on vertical migration of gyrotactic swimmers. Phys. Rev. Fluids 4 (12), 124304. http://dx.doi.org/10.1103/PhysRevFluids.4.124304.

Marchioli, C., Fantoni, M., Soldati, A., 2010. Orientation, distribution, and deposition of elongated, inertial fibers in turbulent channel flow. Phys. Fluids 22 (3), 1–14.

Marchioli, C., Soldati, A., 2002. Mechanisms for particle transfer and segregation in a turbulent boundary layer. J. Fluid Mech. (468), 283–315.

Marchioli, C., Soldati, A., 2013. Rotation statistics of fibers in wall shear turbulence. Acta Mech. 224 (3), 2311–2329.

Marchioli, C., Soldati, A., Kuerten, J.G.M., Arcen, B., Tanière, A., Goldensoph, G., Squires, K.D., Cargnelutti, M.F., Portela, L.M., 2008. Statistics of particle dispersion in direct numerical simulations of wall-bounded turbulence: Results of an international collaborative benchmark test. Int. J. Multiph. Flow. 34 (9), 879–893.

Marchioli, C., Zhao, L., Andersson, H.I., 2016. On the relative rotational motion between rigid fibers and fluid in turbulent channel flow. Phys. Fluids 28 (1), 013301. http://dx.doi.org/10.1063/1.4937757.

Maxey, M.R., 1987. The gravitational settling of aerosol particles in homogeneous turbulence and random flow fields. J. Fluid Mech. 174, 441–465. http://dx.doi.org/10.1017/S0022112087000193.

Maxey, M.R., Riley, J.J., 1983. Equation of motion for a small rigid sphere in a nonuniform flow. Phys. Fluids (26), 883–889.

Michel, A., Arcen, B., 2021. Reynolds number effect on the concentration and preferential orientation of inertial ellipsoids. Phys. Rev. Fluids 6, 114305. http://dx.doi.org/10.1103/PhysRevFluids.6.114305, URL: https://link.aps.org/doi/10.1103/PhysRevFluids.6.114305.

Milici, B., De Marchis, M., 2016. Statistics of inertial particle deviation from fluid particle trajectories in horizontal rough wall turbulent channel flow. Int. J. Heat Fluid Flow 60, 1–11.

Milici, B., De Marchis, M., Sardina, G., Napoli, E., 2014. Effects of roughness on particle dynamics in turbulent channel flows: A DNS analysis. J. Fluid Mech. 739, 465–478.

Mortensen, P.H., Andersson, H.I., Gillissen, J.J., Boersma, B.J., 2008. Dynamics of prolate ellipsoidal particles in a turbulent channel flow. Phys. Fluids 20 (9), 1–14.

Napoli, E., Armenio, V., De Marchis, M., 2008. The effect of the slope of irregularly distributed roughness elements on turbulent wall-bounded flows. J. Fluid Mech. 613, 385–394.

Parsheh, M., Brown, M., Aidun, C., 2005. On the orientation of stiff fibres suspended in turbulent flow in planar contraction. J. Fluid Mech. 545, 245–269.

Qiu, J., Marchioli, C., Andersson, H.I., Zhao, L., 2019. Settling tracer spheroids in vertical turbulent channel flows. Int. J. Multiph. Flow. (ISSN: 0301-9322) 118, 173–182. http://dx.doi.org/10.1016/j.ijmultiphaseflow.2019.06.012, URL: https://www.sciencedirect.com/science/article/pii/S0301932219302186.

Ravnik, J., Marchioli, C., Soldati, A., 2018. Application limits of Jeffery's theory for elongated particle torques in turbulence: a DNS assessment. Acta Mech. 229 (2).

Reeks, M.W., 1983. The transport of discrete particles in inhomogeneous turbulence. J. Aerosol Sci. (ISSN: 0021-8502) 14 (6), 729–739. http://dx.doi.org/10.1016/0021-8502(83)90055-1, URL: https://www.sciencedirect.com/science/article/pii/0021850283900551.

Riemer, N., West, M., Zaveri, R.A., Easter, R.C., 2009. Simulating the evolution of soot mixing state with a particle-resolved aerosol model. J. Geophys. Res.: Atmos. 114 (D9), http://dx.doi.org/10.1029/2008JD011073, URL: https://agupubs.onlinelibrary.wiley.com/doi/abs/10.1029/2008JD011073.

Rouson, D.W.I., Eaton, J.K., 2001. On the preferential concentration of solid particles in turbulent channel flow. J. Fluid Mech. 428, 149–169.

Sardina, G., Picano, F., Schlatter, P., Brandt, L., Casciola, C., 2011. Large scale accumulation patterns of inertial particles in wall-bounded turbulent flow. Flow Turbul. Combust. 86 (3-4), 519–532.

Soldati, A., Marchioli, C., 2009. Physics and modelling of turbulent particle deposition and entrainment: Review of a systematic study. Int. J. Multiph. Flow. (ISSN: 0301-9322) 35 (9), 827–839. http://dx.doi.org/10.1016/j.ijmultiphaseflow.2009.02.016, URL: https://www.sciencedirect.com/science/article/pii/S0301932209000329 Special Issue: Point-Particle Model for Disperse Turbulent Flows.

Sozza, A., Cencini, M., Musacchio, S., Boffetta, G., 2020. Drag enhancement in a dusty Kolmogorov flow. Phys. Rev. Fluids 5, 094302. http://dx.doi.org/10.1103/PhysRevFluids.5.094302, URL: https://link.aps.org/doi/10.1103/PhysRevFluids.5.094302.

Sumbekova, S., Cartellier, A., Aliseda, A., Bourgoin, M., 2017. Preferential concentration of inertial sub-Kolmogorov particles: The roles of mass loading of particles, Stokes numbers, and Reynolds numbers. Phys. Rev. Fluids 2, 024302. http://dx.doi.org/10.1103/PhysRevFluids.2.024302, URL: https://link.aps.org/doi/10.1103/PhysRevFluids.2.024302.

Tenneti, S., Subramaniam, S., 2014. Particle-resolved direct numerical simulation for gas-solid flow model development. Annu. Rev. Fluid Mech. 46 (1), 199–230. http://dx.doi.org/10.1146/annurev-fluid-010313-141344.

Townsend, A.A., 1976. The structure of turbulent shear flow. ZAMM - J. Appl. Math. Mech. / Z. Angew. Math. Mech. 56 (9), 448.

Volino, R.J., Schultz, M.P., Flack, K.A., 2011. Turbulence structure in boundary layers over periodic two- and three- dimensional roughness. J. Fluid Mech. (August 2015).

Voth, G., Soldati, A., 2017. Anisotropic particles in turbulence. Annu. Rev. Fluid Mech. 49, 249–276. http://dx.doi.org/10.1146/annurev-fluid-010816-060135.

Vreman, A.W., 2015. Turbulence attenuation in particle-laden flow in smooth and rough channels. J. Fluid Mech. 773, 103–136. http://dx.doi.org/10.1017/jfm.2015.208.

Wang, J., Zhang, M., Feng, L., Yang, H., Wu, Y., Yue, G., 2020. The behaviors of particle-wall collision for non-spherical particles: Experimental investigation. Powder Technol. (ISSN: 0032-5910) 363, 187–194. http://dx.doi.org/10.1016/j.powtec.2019.12.041, URL: https://www.sciencedirect.com/science/article/pii/S0032591019311465.

Yang, K., Zhao, L., Andersson, H.I., 2020. Orientation of inertial spheroids in turbulent Couette–Poiseuille flow with a shear-free wall. Int. J. Multiph. Flow. (ISSN: 0301-9322) 132, 103411. http://dx.doi.org/10.1016/j.ijmultiphaseflow.2020.103411, URL: https://www.sciencedirect.com/science/article/pii/S0301932220305206.

Zhang, H., Ahmadi, G., Fan, F.G., McLaughlin, J.B., 2001. Ellipsoidal particles transport and deposition in turbulent channel flows. Int. J. Multiph. Flow. 27 (6), 971–1009.

Zhang, B., Xu, D., Zhang, B., Ji, C., Munjiza, A., Williams, J., 2020. Numerical investigation on the incipient motion of non-spherical sediment particles in bedload regime of open channel flows. Comput. Part. Mech. 7, 987–1003.

Zhao, L., Challabotla, N.R., Andersson, H.I., Variano, E.A., 2015. Rotation of nonspherical particles in turbulent channel flow. Phys. Rev. Lett. 115, 244501. http://dx.doi.org/10.1103/PhysRevLett.115.244501, URL: https://link.aps.org/doi/10.1103/PhysRevLett.115.244501.

Zhao, L., Marchioli, C., Andersson, H.I., 2014. Slip velocity of rigid fibers in turbulent channel flow. Phys. Fluids 26 (6), 063302. http://dx.doi.org/10.1063/1.4881942.

Zhao, F., van Wachem, B.G.M., 2013. Direct numerical simulation of ellipsoidal particles in turbulent channel flow. Acta Mech. 224 (10), 2331–2358.